ACS APPLIED MATERIALS & INTERFACES

www.acsami.org
Research Article

Ultrasound-Triggered NPC1L1-Targeting Nanobubbles for Remodeling the Tumor Microenvironment in Pancreatic Cancer Chemoimmunotherapy

Li Dong, Deng Liu, Jun Zhang, Yi Ling, Xin Li, Juanjuan Ou,* and Yanli Guo*

Cite This: ACS Appl. Mater. Interfaces 2025, 17, 34965−34981
Read Online

ACCESS | Metrics & More | Article Recommendations | Supporting Information

ABSTRACT: Abnormal cholesterol metabolism promotes the immunosuppressive microenvironment of pancreatic cancer and affects the long-term efficacy of chemotherapy drugs. Accurate diagnosis and targeted microenvironment-remodeling are challenging during the asymptomatic phase, considerably weakening the antitumor response. To modulate the cholesterol uptake pathway in pancreatic cancer, we developed a seamless diagnostic and chemoimmunotherapy system comprising gemcitabine-loaded nanobubbles with a cholesterol component shell (CHOL@GEM-NBs) fabricated to target the cholesterol transporter Niemann-Pick C1-like 1 (NPC1L1) precisely. The system achieved sufficient permeability to enhance the targeted accumulation of NBs extravasation in tumor blood vessels to locate the tumor region. The CHOL@GEM-NBs exhibited excellent ultrasound molecular imaging performance, with increased contrast intensity and duration time. Moreover, we employed ultrasound-targeted nanobubble destruction (UTND) to facilitate cytotoxicity by enhancing cellular uptake and drug release. This approach reduced NPC1L1 expression and mitigated cholesterol hijacking by tumor cells in the microenvironment. Additionally, ultrasound and cavitation triggered immunogenic cell death to release damage-associated molecular patterns. Essential cholesterol flow restoration and adaptive immunity activation improved the immunosuppressive microenvironment, as evidenced by the increased infiltration of $CD8^+$ cytotoxic T lymphocytes, increased cytokine secretion, decreased proportion of regulatory T cells in tumor tissues, and increased proportions of $CD45^+$, $CD3^+$, and $CD8^+$ T cells in the spleen and draining lymph nodes. In conclusion, the combined CHOL@GEM-NBs and UTND strategy can effectively permeate and reshape the immunosuppressive microenvironment, offering a novel integrated approach for the early diagnosis and chemoimmunotherapy of pancreatic cancer.

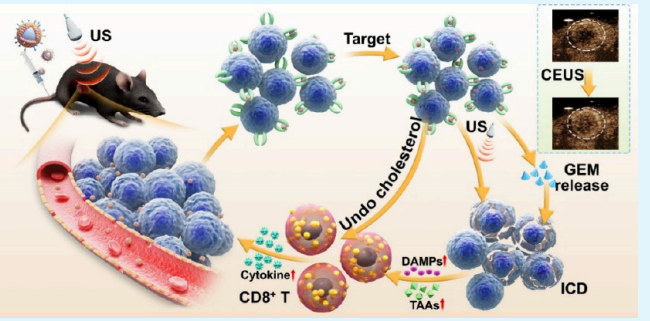

KEYWORDS: *targeted drug-loaded nanobubbles, NPC1L1, pancreatic cancer, ultrasound-targeted nanobubble destruction, tumor microenvironment*

INTRODUCTION

Pancreatic cancer is a serious threat to human health and life due to its dismal prognosis, and the 5-year survival rate is less than 10%.[1,2] Diagnosing the condition in its asymptomatic stage is challenging, as symptoms typically emerge only after the tumor invades surrounding tissues or metastasizes to other organs.[3−5] Unfortunately, pancreatic cancer shows a poor response to conventional chemotherapy, largely due to the ineffective accumulation of therapeutic agents at the tumor site.[6,7] Recently, immunotherapies have been in clinical use for pancreatic cancer, but their therapeutic effects are not satisfactory owing to the immunosuppressive tumor microenvironment (ITM).[8] Hence, a novel strategy for the early diagnosis of pancreatic cancer and remodeling the ITM to enhance therapeutic efficiency is urgently required.

Evidence suggests that disorders of cholesterol metabolism aggravate the ITM in pancreatic cancer.[9] High cholesterol levels in the pancreatic tumor cell membrane surface reduces fluidity and permeability, prevents antineoplastic drug uptake,[10] and promotes proliferation and metastasis.[11] They also result in the upregulation of immune checkpoints, such as programmed death ligand 1 (PD-1), and aggravate T-cell exhaustion.[12] Furthermore, tumor cells subvert T-cell immunity by reprogramming cholesterol metabolism and depleting cholesterol from T cells, thereby sustaining ITM and driving malignant progression.[13,14] Therefore, targeting cholesterol metabolism to remodel the ITM may be an attractive approach.[15,16] Niemann-Pick C1-like 1 (NPC1L1) is a key cholesterol transporter.[17−19]

Received: January 16, 2025
Revised: May 24, 2025
Accepted: May 28, 2025
Published: June 6, 2025

Scheme 1. Structure of CHOL@GEM-NBs and the Mechanism of CHOL@GEM-NBs Combined with UTND Treatment in Pancreatic Cancer

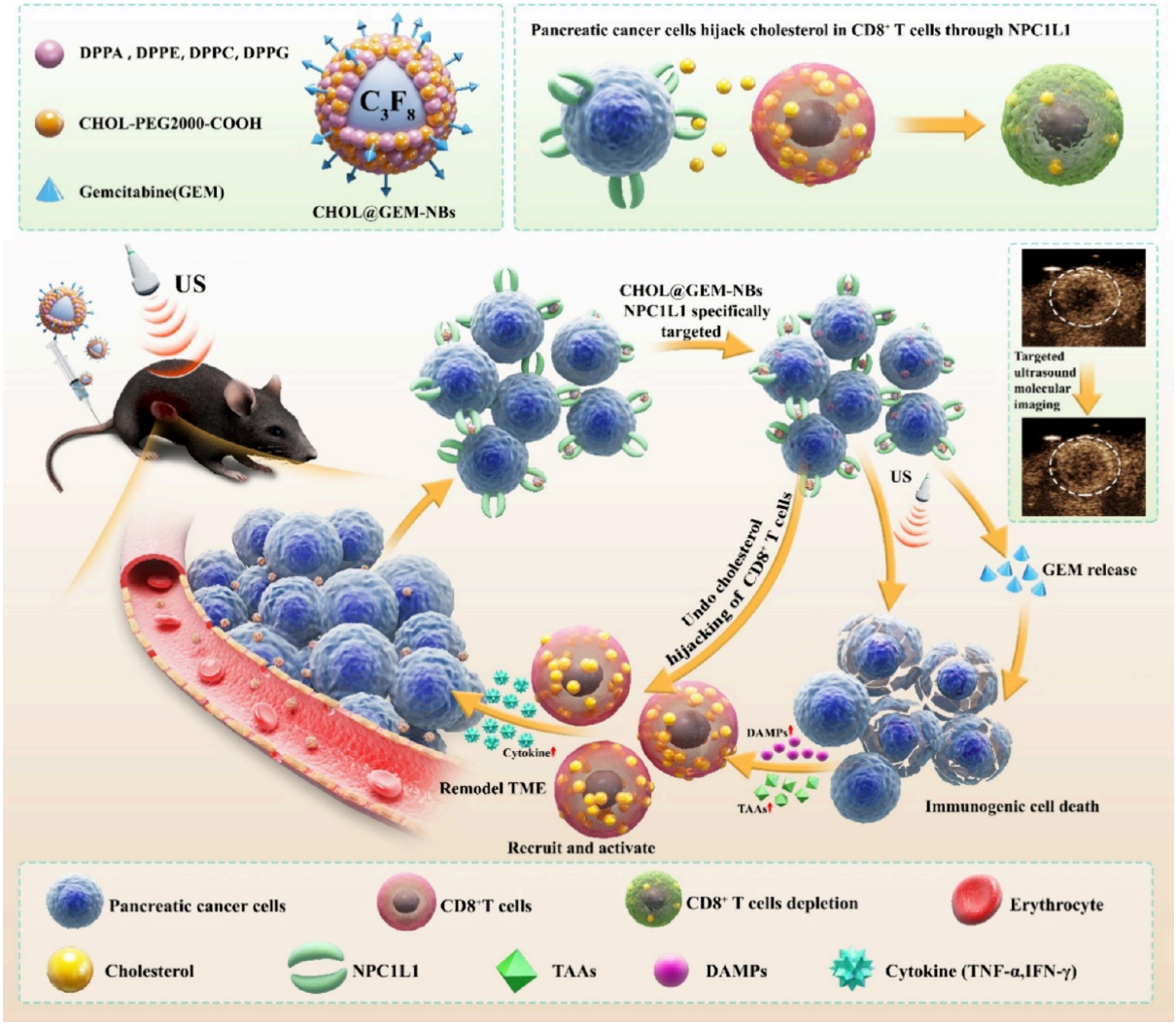

It is aberrantly expressed on the surface of pancreatic cancer cells and is associated with a malignant phenotype, leading to poor overall survival.[20] Recently, microbubbles with large particle diameters (~1−10 μm) were found to be confined to the blood pool, whereas nanobubbles (~100−500 nm), which are smaller, were found to be stable enough to effectively accumulate in the tumor via vascular extravasation.[21−23] Therefore, it is speculated that nanobubbles targeting the NPC1L1-mediated cholesterol uptake pathway enable seamless integration of diagnosis and alter cholesterol flow to regulate the ITM.

Immunotherapy driven by tumor immunogenic cell death (ICD) has been extensively studied.[24,25] Our previous study confirmed that ultrasound-enhanced nanobubble rupture and tumor cell disintegration promote the release of autoantigens in situ, thereby triggering ICD, promoting damage-associated molecular patterns (DAMPs) release, stimulating tumor antigen-specific T cell activation, and further promoting antitumor immune responses.[26] The combination of immunotherapy and chemotherapy is a hot research topic.[27] Enhancing immunogenicity may boost the long-term efficacy of chemotherapy.[28] Therefore, we used ultrasound-targeted nanobubble destruction (UTND) to release the first-line chemotherapy drug gemcitabine (GEM) in order to increase penetration through ultrasound-enhanced cavitation effects, aiming for achieving the maximum lethality against tumor cells.[29−31] Furthermore, the tumor cell lysates after UTND can release tumor-specific antigens for use as in situ vaccines to activate the immune system.[32]

Based on these concepts, we constructed cholesterol-coated nanobubbles loaded with GEM (CHOL@GEM-NBs) that target cholesterol transporter NPC1L1 on the membrane of pancreatic cancer cells (Scheme 1). The cholesterol uptake pathway mediated by NPC1L1 enhances the targeting ability and achieves superior ultrasound molecular imaging for diagnosing pancreatic cancer. We then combined CHOL@GEM-NBs for precise GEM release with UTND to enhance chemotherapeutic effects. Our strategy increased the cellular uptake rate of tumor cells in vitro and promoted efficient accumulation in tumor tissues, thereby inhibiting tumor growth in vivo. Moreover, the treatment effectively promoted adaptive immune response-induced T-cell infiltration and its derived effector cytokines while reducing the proportion of regulatory T cells (Tregs), which led to an antitumor immune response and reshaped the ITM. Additionally, the treatment was highly biocompatible and exhibited no toxicity in tumor-laden mice. In

https://doi.org/10.1021/acsami.5c01194
ACS Appl. Mater. Interfaces 2025, 17, 34965−34981

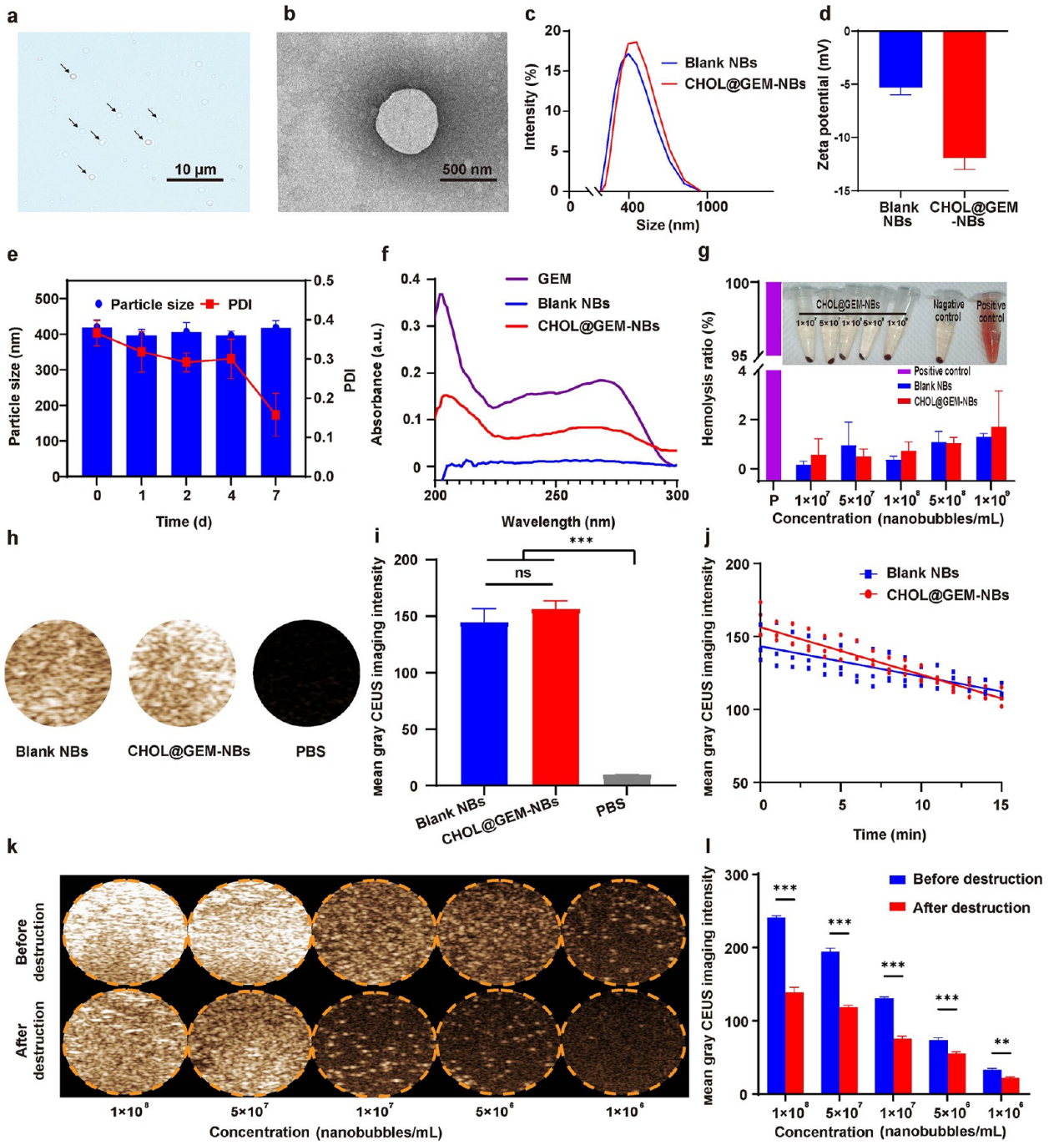

Figure 1. Characterization and performance of CHOL@GEM-NBs. (a, b) Optical microscopy and transmission electron microscopy images of CHOL@GEM-NBs (black arrows). (c) Particle size distribution and (d) zeta potential of CHOL@GEM-NBs and blank NBs. (e) Stability assessment of the hydrodynamic diameter and polydispersity index of CHOL@GEM-NBs (n = 3). (f) Ultraviolet−visible absorption curves of GEM, blank NBs, and CHOL@GEM-NBs at 270 nm. (g) Photograph showing hemolysis of CHOL@GEM-NBs coincubated with red blood cells (PBS and 0.1% Triton X-100 functioned as negative and positive control, respectively) and calculation of the hemolysis rate (n = 3). (h) Contrast-enhanced ultrasound images of CHOL@GEM-NBs, blank NBs, and PBS in vitro. (i) Statistics of intensity value calculated from contrast-enhanced ultrasound images. (j) Decay rate of CHOL@GEM-NBs and blank NBs in vitro. (k, l) CHOL@GEM-NBs contrast-enhanced ultrasound images before and after destruction at different concentrations (n = 3). Data are shown as mean ± SD *P < 0.05, **P < 0.01, and ***P < 0.001.

conclusion, CHOL@GEM-NBs represent a safe and promising strategy for diagnosing and treating pancreatic cancer.

RESULTS

Characterization and Performance of CHOL@GEM-NBs. Scheme 1 presents a schematic of CHOL@GEM-NBs formation. Cholesterol was incorporated into the lipid shell of the NBs and the chemotherapeutic drug GEM was covalently linked to the cholesterol (Figures S1 and 2). Optical microscopy images revealed uniformly dispersed nanobubbles exhibiting spherical morphology (Figure 1a), and transmission electron microscopy further confirmed the potential core−shell architecture (Figure 1b). The concentration of CHOL@GEM-NBs was determined as (9.84 ± 0.77) × 10^{10}/mL via

https://doi.org/10.1021/acsami.5c01194
ACS Appl. Mater. Interfaces 2025, 17, 34965−34981

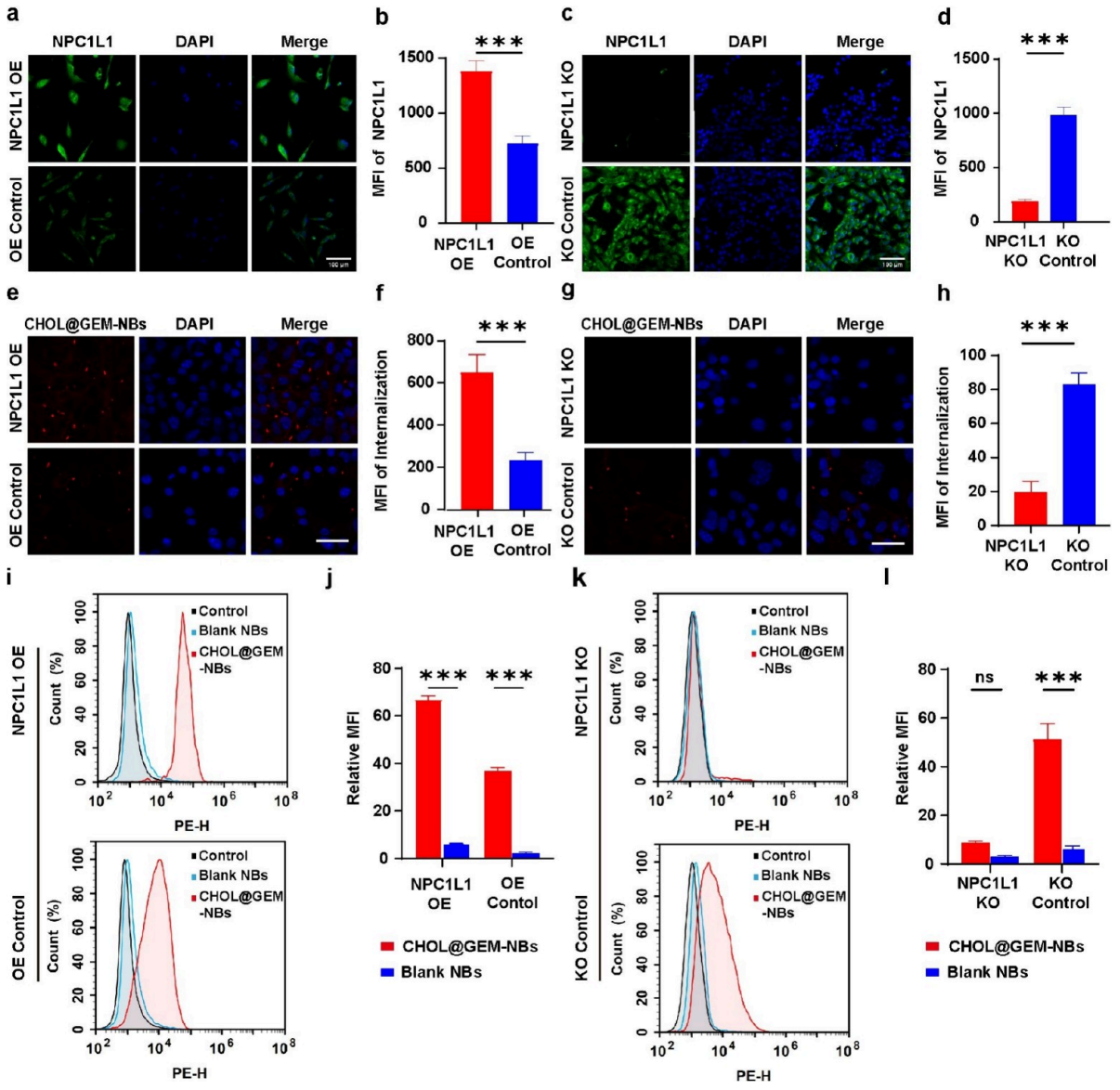

Figure 2. Binding specificity for NPC1L1. (a–d) NPC1L1 expression of NPC1L1 OE and OE control cells (a and b), and NPC1L1 KO and KO control cells (c and d) via a CLSM (scale bar = 100 μm, n = 3). (e–h) Immunofluorescence imaging and quantitative analysis of binding specificity between CHOL@GEM-NBs and (e and f) NPC1L1 KO, KO control, (g and h) NPC1L1 OE, and OE control cells (scale bar = 50 μm). (i–l) Quantitative analysis of NBs intracellular uptake (CHOL@GEM-NBs or blank NBs) by (i and j) NPC1L1 OE and OE control cells and (k and l) NPC1L1 KO and KO control cells (n = 3). Data are shown as mean ± SD *P < 0.05, **P < 0.01, and ***P < 0.001.

optical microscopy. According to dynamic light scattering analysis, blank NBs and CHOL@GEM-NBs displayed an average hydrodynamic diameter of 380.24 ± 13.27 and 419.5 ± 20.34 nm (Figure 1c) and a zeta potential of −5.33 ± 0.65 and −11.93 ± 1.07 mV, respectively (Figure 1d). A negative zeta potential guarantees that NBs maintain their uniform dispersion in circulation and enhances their stability.[33] The increase in diameter and change in charge indirectly validated the successful loading of cholesterol and encapsulation of GEM. The NBs demonstrated outstanding stability when stored at 4 °C for prolonged periods. No substantial differences in the particle size of CHOL@GEM-NBs were observed among multiple time points (1, 2, 4, and 7 days) (Figure 1e).

A characteristic absorption peak at ∼270 nm, ascribed to GEM, was observed in the CHOL@GEM-NBs ultraviolet–visible absorption spectrum (Figures 1f and S3). Ultraviolet–visible spectroscopy confirmed the successful encapsulation of GEM within the NBs, with quantitative measurements revealing a GEM concentration of 48.80 ± 1.20 μg/mL, encapsulation efficiency of 53.81 ± 1.08%, and drug loading capacity of 4.436 ± 0.09%. Subsequent assessments focused on NBs safety. The hemolysis rates were below 5% for all concentrations (1×10^7, 5×10^7, 1×10^8, 5×10^8, and 1×10^9/mL) of NBs and CHOL@GEM-NBs coincubated with red blood cells, indicating in vitro biocompatibility of NBs during drug delivery (Figure 1g). Furthermore, comprehensive biochemical analyses and histological evaluations of Panc02 tumor-laden C57BL/6 mice to assess the in vivo biosafety of GEM and NBs revealed no notable changes in routine blood (Table S1), liver function, or renal function test results (Figure S4). These results suggested that CHOL@GEM-NBs did not exert significant toxic effects on the hematological system or organs. Additionally, pathological alterations in the major organs (heart, liver, spleen, lung, and kidney) of the mice via hematoxylin and eosin (H&E) staining

https://doi.org/10.1021/acsami.5c01194
ACS Appl. Mater. Interfaces 2025, 17, 34965–34981

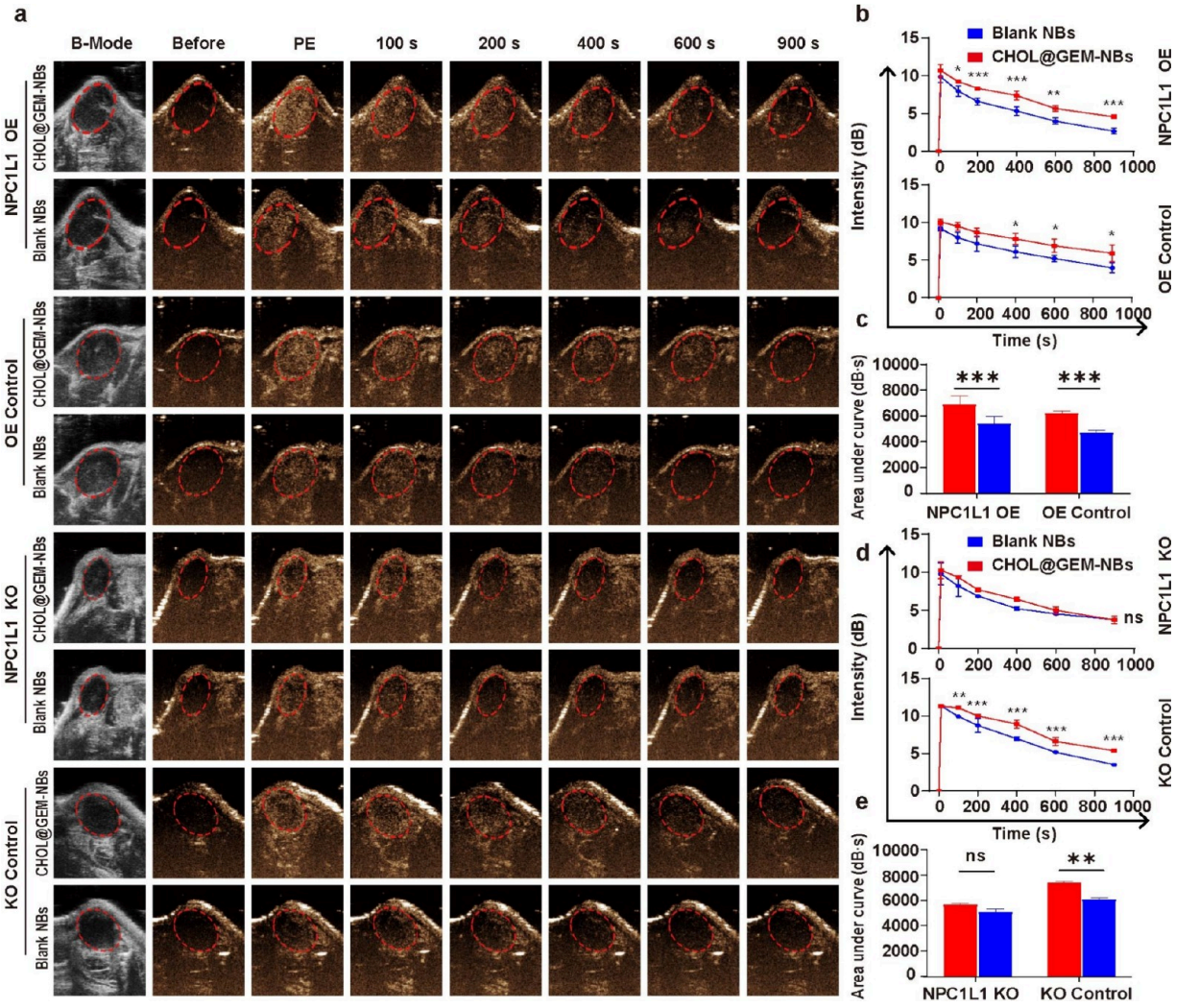

Figure 3. CHOL@GEM-NBs ultrasound molecular imaging performance. (a) Contrast-enhanced ultrasound imaging of different NBs (CHOL@GEM-NBs and blank NBs) in NPC1L1 OE, OE control, NPC1L1 KO, and KO control cells in tumor-laden mice. The experiment was independently repeated twice with comparable results. (b and d) Time−intensity curves of CHOL@GEM-NBs and blank NBs in (b) NPC1L1 OE, OE control, (d) NPC1L1 KO, and KO control cells ($n = 3$). (c and e) Area under the time−intensity curve between CHOL@GEM-NBs and blank NBs in (c) NPC1L1 OE, OE control, (e) NPC1L1 KO, and KO control cells ($n = 3$). Data are shown as mean ± SD $^*P < 0.05$, $^{**}P < 0.01$, and $^{***}P < 0.001$.

indicated no notable histological changes (Figure S5). No abnormal changes in body weight were observed in any treatment group (Figure S6). These findings implied that CHOL@GEM-NBs demonstrated excellent biocompatibility and safety in vivo. This is promising for tumor treatment and offers substantial support for the clinical translation of CHOL@GEM-NBs.

In the agarose model, both CHOL@GEM-NBs and blank NBs exhibited superior contrast-enhanced ultrasound intensity compared to phosphate-buffered saline (PBS) (Figure 1h−i). They displayed progressive signal attenuation during 15 min ultrasound monitoring, with no statistically significant difference in decay rates, indicating comparable in vitro stability profiles. (Figure 1j). Thus, the intensity of ultrasound imaging of CHOL@GEM-NBs (before destruction) was positively correlated with the concentration (Figure 1k). After producing cavitated and ruptured NBs, a significant reduction in ultrasound imaging intensity was observed via reperfusion imaging in CHOL@GEM-NBs (after destruction) (Figure 1l), indicating that the ultrasound-mediated destruction of NBs disrupted their integrity, allowing drug release at specific tumor sites.

Binding Specificity of CHOL@GEM-NBs to NPC1L1. The active targeting and efficient accumulation of a nanoplatform are key to achieving accurate diagnosis and effective therapy.[34] NPC1L1 expression in different cells (NPC1L1 OE, OE control, NPC1L1 KO and KO control) was assessed using a confocal laser microscope (CLSM). Green fluorescence was observed in NPC1L1-positive cells, whereas almost no green fluorescence was observed in NPC1L1 KO cells (Figure 2a,c). Quantitative analysis revealed a significant difference in NPC1L1 expression between the two groups (Figure 2b,d). The binding specificity of CHOL@GEM-NBs to Panc02 cells was evaluated using a CLSM (Figure 2e,g). Compared to NPC1L1 KO cells, which do not express NPC1L1, abundant DiI-labeled CHOL@GEM-NBs were observed around pancreatic cancer cells with NPC1L1 expression (Figure 2f,h). These results indicate that the number of DiI-targeted NBs binding was proportional to NPC1L1 expression on the membrane surface of the cells. In contrast, few DiI-labeled blank NBs were detected in the four cell lines (Figure S7). Flow cytometry revealed that the

https://doi.org/10.1021/acsami.5c01194
ACS Appl. Mater. Interfaces 2025, 17, 34965−34981

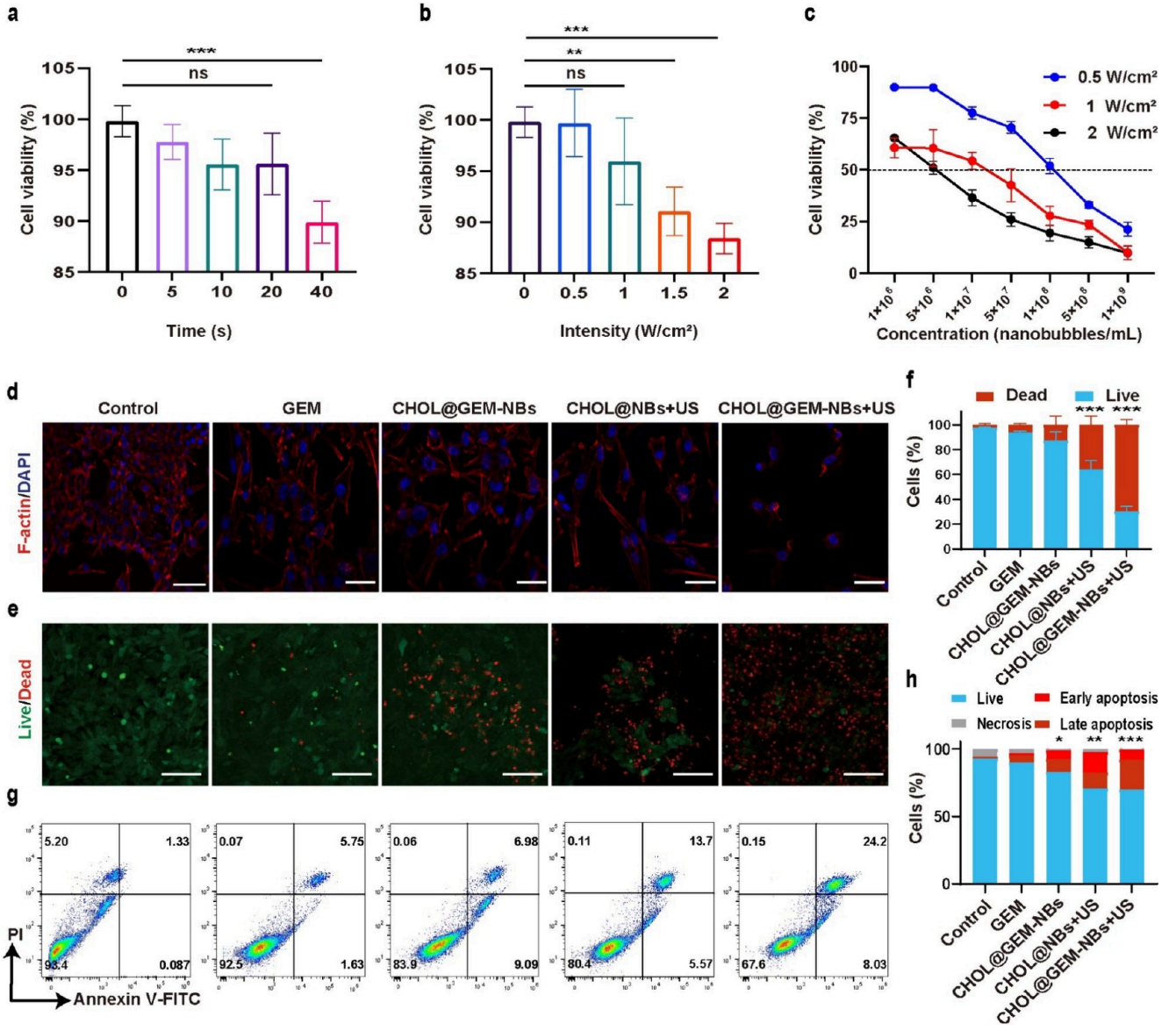

Figure 4. UTND enhanced the cytotoxicity of CHOL@GEM-NBs. (a–c) Screening of the optimal (a) ultrasound irradiation time (n = 4), (b) ultrasound irradiation intensity (n = 4), and (c) nanobubble concentration combined with ultrasound irradiation (n = 4). (d) F-actin and DAPI immunofluorescent images of Panc02 cells in the different treatment groups as assessed using a CLSM (scale bar = 100 μm). (e) Live/dead fluorescent images of Panc02 cells in the different treatment groups as assessed using a CLSM (scale bar = 100 μm). (f) Quantification of the live/dead cell ratio from Panc02 cells in each treatment group (n = 3). (g) Quantitative analysis of the apoptosis of Panc02 cells for each treatment group. (h) Flow cytometric results depicting apoptosis in the different treatment groups (n = 3). Data are shown as the mean ± SD *P < 0.05, **P < 0.01, and ***P < 0.001 vs the control group.

cellular uptake of CHOL@GEM-NBs by NPC1L1 OE cells or NPC1L1 KO control cells was significantly greater than that by NPC1L1 OE control cells or NPC1L1 KO cells (Figure 2i,k). Quantitative analysis showed that the binding rates of CHOL@GEM-NBs and blank NBs were 67.0 ± 1.4% vs 6.3 ± 0.3% for NPC1L1 OE cells, 37.9 ± 1.4% vs 2.3 ± 0.3% for NPC1L1 OE control cells, and 51.4 ± 6.2% vs 6.0 ± 1.4% for NPC1L1 KO control cells. Conversely, we observed no significant difference in affinity to NPC1L1 KO cells between CHOL@GEM-NBs and blank NBs (Figure 2j,l). These findings prove that cholesterol-modified CHOL@GEM-NBs can specifically target NPC1L1-expressing Panc02 cells. Therefore, NPC1L1 is an ideal target for diagnosing and treating pancreatic cancer. The specific active targeting of CHOL@GEM-NBs enables the precise delivery and effective accumulation in tumor tissues, which contributes to enhanced therapeutic efficacy in tumor treatment while minimizing adverse effects.

Ultrasound Molecular Imaging Performance of CHOL@GEM-NBs. Given the high expression of NPC1L1 in pancreatic tumors, contrast-enhanced ultrasound imaging capability of CHOL@GEM-NBs was analyzed in tumor-laden mice in vivo. Critical factors for active-targeted tumor imaging are the specific binding and retention of CHOL@GEM-NBs at tumor sites. The acquired images showed that CHOL@GEM-NBs exhibited significant advantages in prolonged imaging time and ultrasound enhancement intensity compared to blank NBs in NPC1L1-positive pancreatic tumors (Figure 3a). According to quantitative analysis of the peak intensity, time to peak intensity, and area under the curve in different cells treated with CHOL@GEM-NBs or blank NBs (Figure 3b–e), the time–

https://doi.org/10.1021/acsami.5c01194
ACS Appl. Mater. Interfaces 2025, 17, 34965–34981

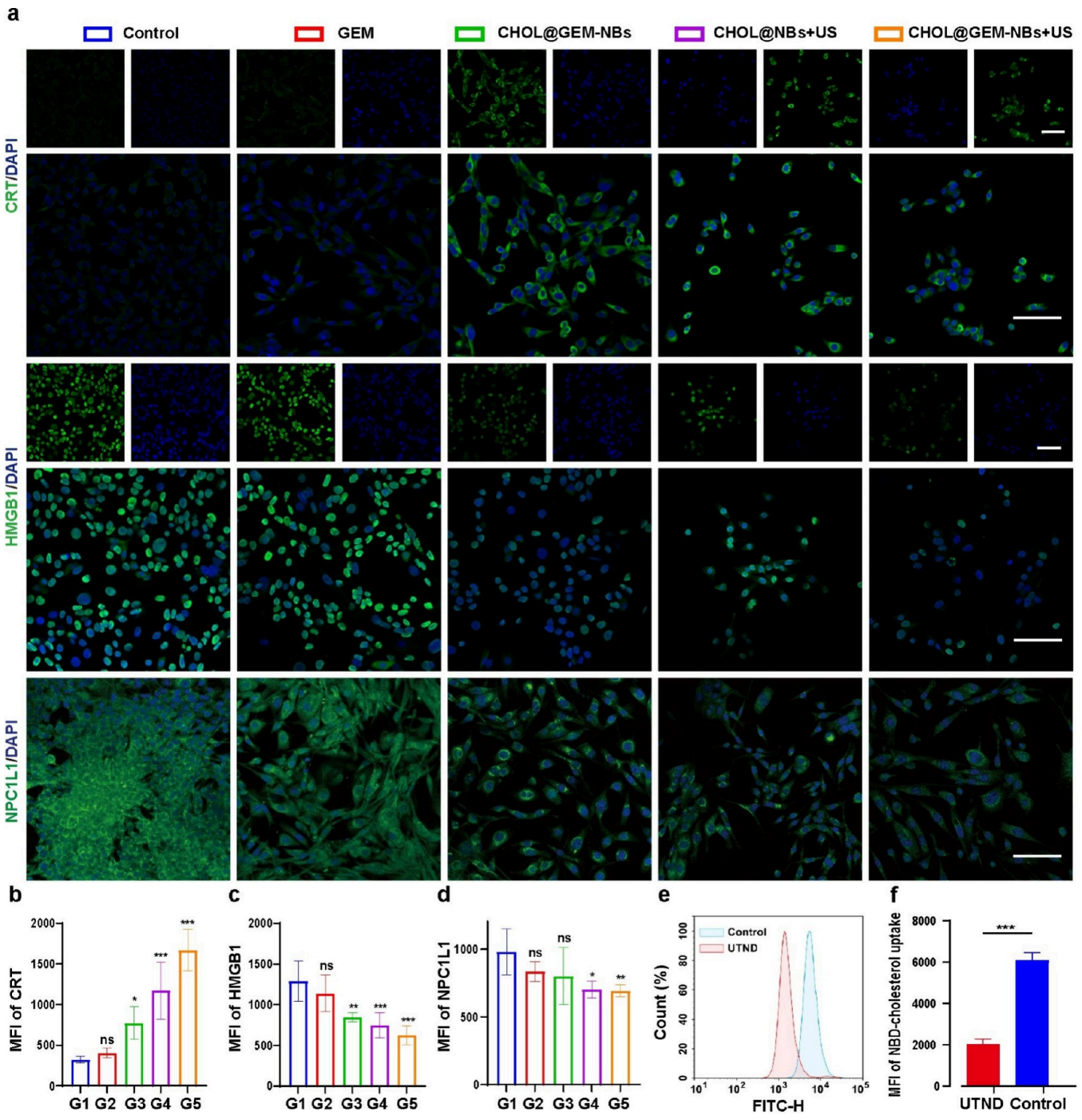

Figure 5. UTND enhances the immunological activity of CHOL@GEM-NBs. (a) CLSM images of CRT, HMGB1, and NPC1L1 expression in Panc02 cells after different treatments (scale bar = 100 μm). (b–d) Mean fluorescence intensity of (b) CRT, (c) HMGB1, and (d) NPC1L1 (n = 3). (e) Flow cytometry histogram of cholesterol uptake in treated panc02 cells. (f) Mean fluorescence intensity of cholesterol uptake (n = 3). Data are shown as mean ± SD *P < 0.05, **P < 0.01, and ***P < 0.001. G1: Control, G2: GEM, G3: CHOL@GEM-NBs, G4: CHOL@NBs + US, G5: CHOL@GEM-NBs + US.

intensity curve rapidly rose to a peak within approximately 10 s (Tables S2 and S3), then began to decline until to 900 s. However, in the NPC1L1 OE, NPC1L1 OE control, and NPC1L1 KO control cells, CHOL@GEM-NBs showed higher ultrasound intensity enhancement. In contrast, weaker signals were observed in the blank NBs, and almost no signal was detected at 900 s. We observed no significant differences in NPC1L1 KO cells treated with CHOL@GEM-NBs and blank NBs. These results showed that the synthesized CHOL@GEM-NBs exhibited more robust targeting and accumulation abilities than nontargeted blank NBs, demonstrating their good clinical potential for diagnosing pancreatic cancer.

UTND Enhanced the Cytotoxicity of CHOL@GEM-NBs. Considering the potential for irreversible cytopathological damage under sustained ultrasound irradiation,[35] the CCK-8 assay was used to assess the cell viability of treatments with ultrasound irradiation to determine the appropriate parameters (Figure 4a–c). Under ultrasound irradiation alone, Panc02 cells

https://doi.org/10.1021/acsami.5c01194
ACS Appl. Mater. Interfaces 2025, 17, 34965–34981

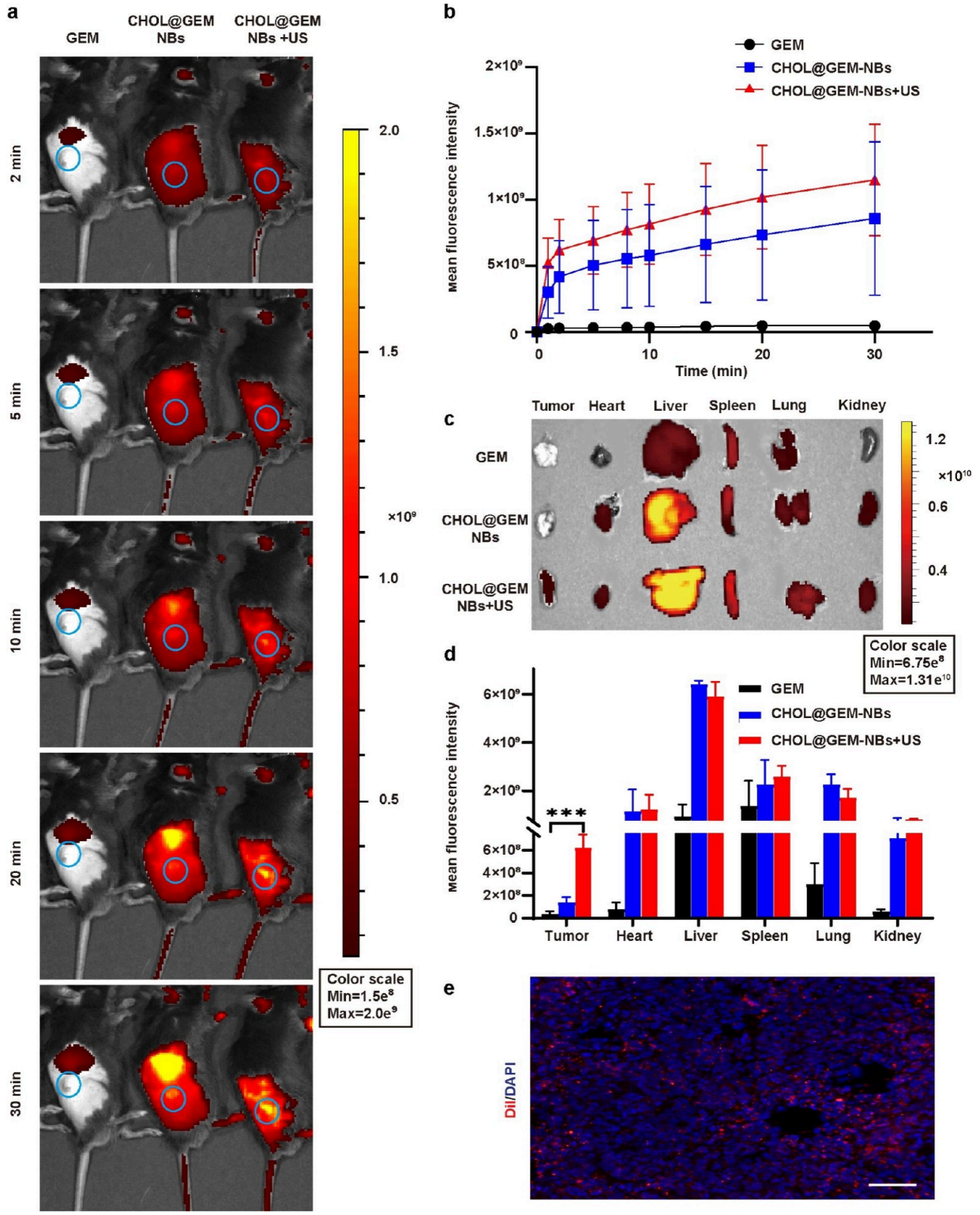

Figure 6. UTND enhanced the targeting ability of CHOL@GEM-NBs. (a) In vivo, fluorescence imaging was conducted on mice with Panc02 cell-laden tumors at different time points following intravenous injection of DiR-labeled GEM, CHOL@GEM-NBs, and CHOL@GEM-NBs + ultrasound irradiation (US). The experiment was independently repeated thrice with comparable results. (b) Mean fluorescence signal intensity of the tumor site in vivo as a function of time. (c) In vitro fluorescence imaging of tumors and vital organs 30 min postintravenous injection. (d) Quantitative assessment of the mean fluorescence intensity in excised tumors and vital organs. (e) Tumor tissue distribution after DiI-CHOL@GEM-NBs + US treatment (scale bar = 50 μm). Data are shown as means ± SD $^{*}P < 0.05$, $^{**}P < 0.01$, and $^{***}P < 0.001$.

demonstrated significant time- and intensity-dependent viability attenuation. Threshold effects were observed when exposure duration reached ≥ 40s or intensity exceeded 1.5 W/cm^2, with significantly reduced viability in Panc02 cells compared to that in untreated control cells (Figure 4a,b). Therefore, subsequent experiments adopted 1 W/cm^2 intensity with 20 s of irradiation

https://doi.org/10.1021/acsami.5c01194
ACS Appl. Mater. Interfaces 2025, 17, 34965−34981

as the optimal ultrasound parameters. Panc02 cells treated with CHOL@GEN-NBs demonstrated a significant concentration-dependent reduction in cell viability under ultrasound irradiation; when the concentration of CHOL@GEN-NBs was 5×10^7/mL, Panc02 cell viability significantly decreased to 42.59 ± 7.87% (Figure 4c).

The cytoskeleton is tightly connected to the cell membrane to support the cell morphology.[36] Changes in the actin cytoskeleton are associated with lamellipodia, which promote cancer cell invasion and metastasis.[37] Different treatment groups had significantly affected lamellipodia formation in Panc02 cells (Figure 4d). In the control and GEM groups, Panc02 cells exhibited a typical fibroblast-like morphology. Considerable amounts of actin aggregates were visible inside the cells with a relatively haphazard, dense, and widespread distribution of F-actin. A large number of pseudopods, which indicate migratory ability, formed at the cell edges. In contrast, in the CHOL@GEM-NBs + US group, F-actin was tightly clustered around the cell nucleus in a sphere and few obvious cell pseudopods were present. Moreover, F-actin underwent significant depolymerization and rearrangement, and its content was significantly reduced compared to that in the other groups.

In addition, live cell staining using calcein−acetoxymethyl (AM) and dead cell staining with propidium iodide (PI) were performed to illustrate the cytotoxicity of Panc02 cells following treatment in the different groups (Figure 4e). Significant red fluorescence was detected in the CHOL@GEM-NBs + US group. In the GEM group, green fluorescence was uniformly distributed in the live cells, whereas only sporadic red fluorescence was observed in the dead cells. Quantitative analysis also proved that the CHOL@GEM-NBs + US group exhibited the most effective antitumor effect (Figure 4f). This is attributed to the higher intracellular uptake efficiency of CHOL@GEM-NBs + US compared to that of GEM. Annexin V-FITC/PI staining consistently confirmed the trend of cell death caused by apoptosis in each group (Figure 4g,h). These results suggest the superiority of CHOL@GEM-NBs + US in treating pancreatic cancer.

UTND Enhanced the Immunological Activity of CHOL@GEM-NBs. DAMPs, such as calreticulin (CRT) and high-mobility group box 1 (HMGB1), serve as biomarkers of ICD. During ICD, CRT is exposed on the surface of dying or stressed cells, acting as a vital "eat me" signal to stimulate the antigen-presenting function and prime the adaptive immune system. Conversely, HMGB1 is released from the nucleus into the extracellular milieu of dying cells as a "danger" signal to activate innate immune cells and generate cytokines, creating a favorable microenvironment for antigen-presenting and T cells.[38] The combined action of CRT and HMGB1 during ICD forms a positive feedback loop, thus enhancing the overall immune response.[39] Cytokines from activated innate immune cells further modulate CRT and HMGB1, strengthening their roles. This coordinated action is vital for eliminating damaged or tumorigenic cells and establishing long-term immune memory.[25,40]

CRT expression was upregulated after different treatments, whereas HMGB1 expression was downregulated (Figure 5a). The average fluorescence intensity of CRT was five times higher in the CHOL@GEM-NBs + US group than in the control group. Moreover, compared to the control group, the average fluorescence intensities of CRT in the CHOL@NBs + US group were two times greater, whereas that in the CHOL@NBs + US group was three times greater (Figure 5b). Substantial green fluorescence was observed in the control and GEM groups, and HMGB1 in the CHOL@NBs + US and CHOL@GEM-NBs + US groups showed negligible green fluorescence signals (Figure 5c). These findings indicated that UTND-enhanced CHOL@GEM-NBs can induce ICD and promote DAMPs release.

The inhibitory effect of each treatment group on NPC1L1 expression was determined in Panc02 cells (Figure 5a). Quantitative analysis showed that the GEM and CHOL@GEM-NBs groups did not inhibit NPC1L1 expression compared to the control group, but CHOL@GEM-NBs combined with UTND significantly inhibited NPC1L1 expression (Figure 5d), indicating that CHOL@GEM-NBs + US achieves efficient cellular damage while concurrently reducing cholesterol.

Cancer cells compete for nutrients to meet their rapid growth requirements, including hijacking the cholesterol in immune cells, which weakens antitumor immunity.[13,17] Immunosuppressive cells may accomplish tumor immune evasion owing to their metabolic flexibility to adapt to deprivation of the tumor microenvironment.[15] Therefore, flow cytometry was used to observe the cholesterol uptake ability of tumor cells. Compared with the control group, Panc02 cells treated with CHOL@GEM-NBs + US showed a reduced capacity for cholesterol uptake (Figure 5e). Quantitative analysis showed that the mean fluorescence intensity of cholesterol decreased 3-fold (Figure 5f). These results imply that the ability of tumor cells to hijack cholesterol, an essential nutrient for immune cells, was reduced after treatment with CHOL@GEM-NBs combined with UTND.

UTND Enhanced the Targeting Ability of CHOL@GEM-NBs. Based on the above results, the efficacy of UTND-enhanced CHOL@GEM-NBs was further evaluated and validated. The distribution of DiR-labeled CHOL@GEM-NBs in tumors and internal tissues with UTND was explored using an in vivo imaging system. After intravenous injection of the drugs, the fluorescence intensity at the tumor site in the GEM group was weak and showed no significant change over time. In the CHOL@GEM-NBs and CHOL@GEM-NBs + US groups, the fluorescence intensity in the tumor area (blue circle) of tumor-bearing mice increased with time (Figure 6a). At 30 min, the fluorescence intensity of CHOL@GEM-NBs + US was higher than that of CHOL@GEM-NBs. After 30 min, the main tissues, organs, and tumors were excised and subjected to fluorescence quantification. The fluorescence intensity of the ex vivo tumors in the CHOL@GEM-NBs + US group was significantly higher than that in the CHOL@GEM-NBs and GEM groups, indicating that ultrasound can enhance the CHOL@GEM-NBs accumulation at the tumor site (Figure 6b). This indicates that UTND enhances the passive targeting ability of CHOL@GEM-NBs and promotes the effective accumulation of CHOL@GEM-NBs at tumor sites. Following 30 min of imaging, the fluorescence signal accumulated predominantly in the liver; this phenomenon is attributed to the active uptake of nanoparticles by the reticuloendothelial system (Figure 6c,d). Frozen sections of the tumors treated with DiI-labeled CHOL@GEM-NBs + US were observed using a CLSM (Figure 6e), which revealed abundant CHOL@GEM-NBs accumulated in the tumor tissue. UTND induces a sonoporation effect,[29] which enhances the delivery and accumulation of GEM in tumor tissues. This effect was sustained and stable, indicating great potential for tumor therapy.

https://doi.org/10.1021/acsami.5c01194
ACS Appl. Mater. Interfaces 2025, 17, 34965−34981

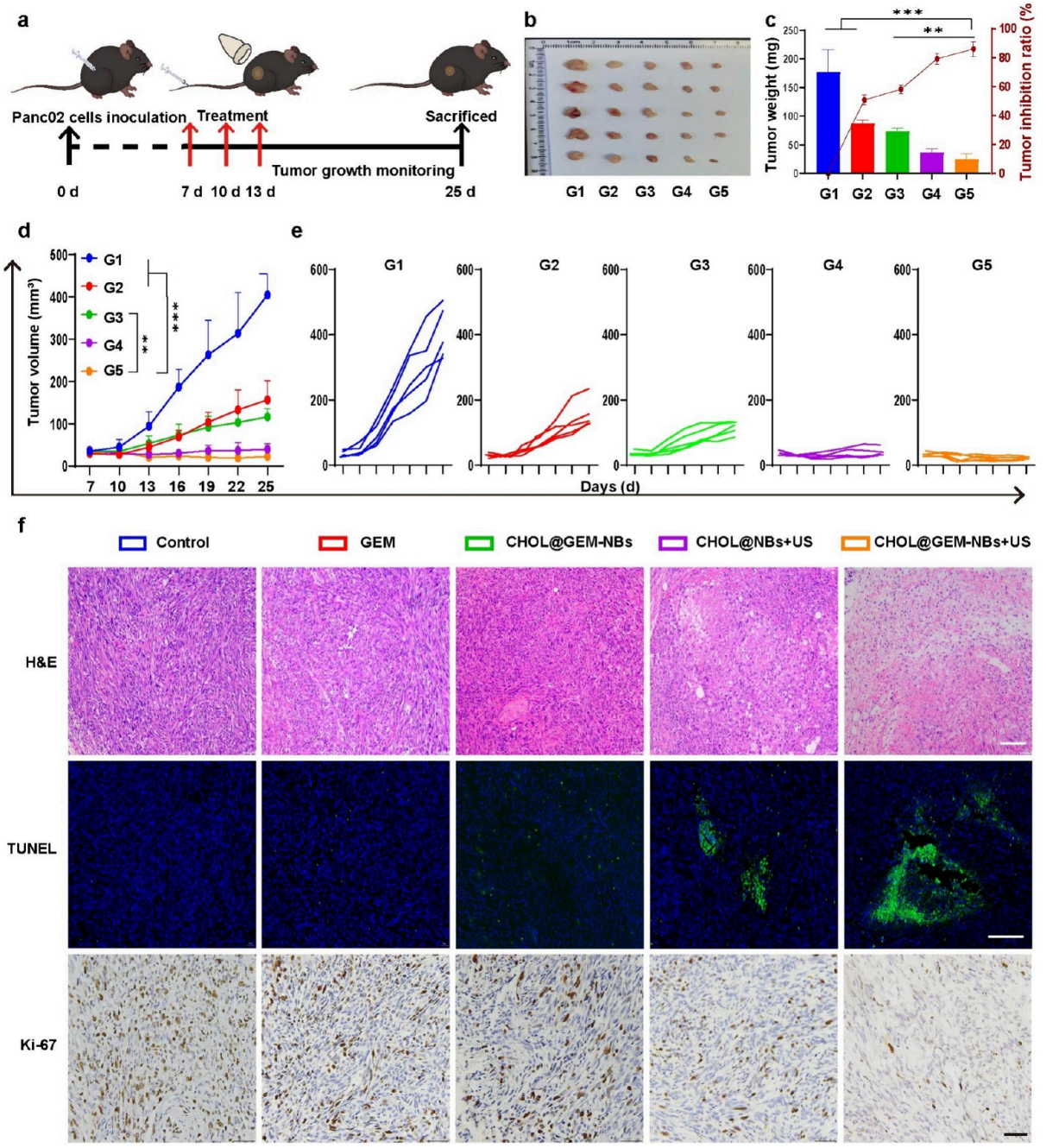

Figure 7. Synergistic antitumor therapy. (a) Schematic representation of the pancreatic tumor model and treatment with CHOL@GEM-NBs and UTND. (b) Images of excised tumors in different treatment groups. (c) Excised tumor weight (bar graph) and inhibition rate (line graph) for the different treatment groups. (d) Average tumor volume changes in the different treatment groups. (e) Individual tumor volumes of tumor-laden mice in each group. (n = 5) (f) H&E, TUNEL, and Ki-67 staining of different treatment groups (scale bar = 100 μm). Data are shown as the mean ± SD *P < 0.05, **P < 0.01, and ***P < 0.001. G1: Control, G2: GEM, G3: CHOL@GEM-NBs, G4: CHOL@NBs + US, G5: CHOL@GEM-NBs + US.

Synergistic Antitumor Therapy of CHOL@GEM-NBs and UTND. Owing to the excellent targeting capacity of CHOL@GEM-NBs + US in vivo, the treatment outcome of the antitumor therapy was analyzed in Panc02 tumor-laden mice (Figure 7a). Mice were administered different treatment regimens, and changes in tumor volume were measured at 25 days (Figure 7d,e). In addition, the treatment effect was assessed by recording photographs of the excised tumor (Figure 7b). Compared with the control group, the CHOL@GEM-NBs + US group achieved an excellent therapeutic effect, with a minimum tumor weight and the inhibition rate was 86% (Figure 7c). Notably, CHOL@NBs + US presented somewhat suboptimal antitumor activity. CHOL@NBs actively target NPC1L1-expressing Panc02 cells and efficiently accumulate in tumor tissues and mediating physical tumor destruction under ultrasound irradiation. In contrast, the GEM group showed a less effective outcome than the CHOL@GEM-NBs group, probably because free GEM lacks tumor-targeting capability and fails to accumulate effectively in tumor tissues. This proved that UTND-enhanced CHOL@GEM-NBs could increase NBs accumulation in the tumor region to achieve a better therapeutic effect.

https://doi.org/10.1021/acsami.5c01194
ACS Appl. Mater. Interfaces 2025, 17, 34965−34981

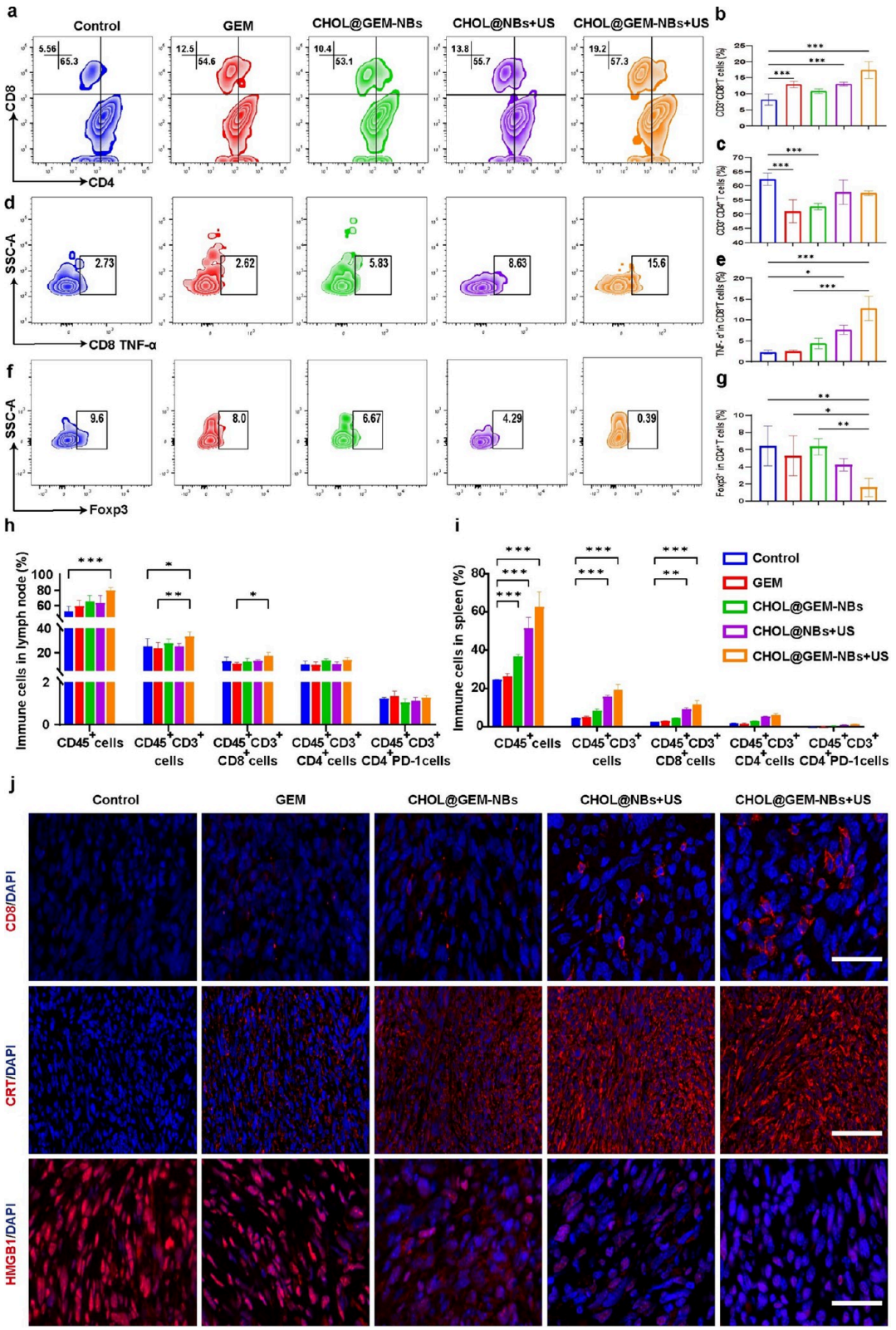

Figure 8. Immune mechanism of synergistic antitumor therapy. (a−g) Representative histograms of flow cytometry and infiltrating leukocytes, including $CD8^+$ T cells in the tumor ($CD45^+CD3^+CD8^+$), $CD4^+$ T cells ($CD45^+CD3^+CD4^+$) (a−c), TNF-α-positive proportions of $CD8^+$ T cells (d, e), and $CD4^+Foxp3^+$ T cells ($CD45^+CD3^+CD4^+Foxp3^+$) (f, g). (h, i) Draining lymph node lymphocytes and immune cells in the spleen, including $CD45^+$ cells, $CD3^+$ T cells ($CD45^+CD3^+$), $CD8^+$ T cells ($CD45^+CD3^+CD8^+$), $CD4^+$ T cells ($CD45^+CD3^+CD4^+$), and PD-1-positive proportions of $CD4^+$ T cells ($CD45^+CD3^+CD4^+PD\text{-}1^+$) ($n = 4$). (j) $CD8^+$ (scale bar = 50 μm), CRT (scale bar = 100 μm), HMGB1 (scale bar = 50 μm), and DAPI immunofluorescent images of tumor tissue in the indicated therapy groups, as detected via a fluorescence microscope. Data are shown as the mean ± SD $^*P < 0.05$, $^{**}P < 0.01$, and $^{***}P < 0.001$.

https://doi.org/10.1021/acsami.5c01194
ACS Appl. Mater. Interfaces 2025, 17, 34965−34981

Next, we performed an immunohistochemical examination of tumor tissues to better understand the synergistic antitumor effects of CHOL@GEM-NBs and UTND in vivo (Figure 7f). CHOL@GEM-NBs + US group exhibited significantly increased necrosis and apoptosis on H&E staining, proliferation suppression in K_i-67 staining, and apoptosis cells in the TUNEL assay. These results indicated a more favorable prognosis. Thus, combining CHOL@GEM-NBs and UTND will likely achieve superior therapeutic effects.

Immune Mechanism of Synergistic Antitumor Therapy. In previous experiments, CHOL@GEM-NBs were combined with UTND to enhance the function of relevant immune cells in vitro. Owing to the intricacy and heterogeneity of the tumor microenvironment, the mechanism through which CHOL@GEM-NBs + US evokes systemic antitumor immunity was further explored. Immune cells within the tumor, draining lymph nodes, and spleen were evaluated after the end of treatment. According to the flow cytometry gating strategy (Figure S8), $CD3^+$ T cells increased within the tumor receiving CHOL@GEM-NBs + US treatment (Figure S9), implying an enhanced immune response. Moreover, the infiltration of $CD8^+$ T cells after treatment was 2.12 times higher than that in the control group, and $CD8^+$ T cells in the CHOL@NBs + US group (13.05 ± 0.57%) were also significantly more abundant than those in the control group (8.19 ± 1.73%) (Figure 8a,b). This effect may be attributed to the fact that UTND-induced cavitation simultaneously promotes DAMPs release and acts synergistically to generate a broad immune response by releasing tumor-associated antigens from tumor cell debris. Cytotoxic $CD8^+$ T lymphocytes are usually inactive in pancreatic tumors, and elevated cytotoxic T lymphocytes are a positive marker for pancreatic cancer prognosis.[41,42] Additionally, activated immune cells can secrete proinflammatory cytokines, which are typical markers of upregulated antitumor immune responses.[43] Furthermore, the TNF-α expression associated with $CD8^+$ T cell activation was the highest in tumors treated with CHOL@GEM-NBs + US (Figure 8d,e), further confirming that the combination of CHOL@GEM-NBs and UTND enhanced the infiltration of $CD8^+$ T cells within the tumor. However, we did not observe a significant increase in the expression levels of $CD4^+$ T cells in the CHOL@GEM-NBs + US group (Figure 8c), and the frequency of immunosuppressive Tregs ($CD4^+Foxp3^+$) was decreased (Figure 8f,g), indicating remission of the tumor immunosuppressive microenvironment.[44,45]

To determine systemic immune response activation, we further examined the percentage of immune cells in the spleen and draining lymph nodes (Figure 8h,i). CD45, CD3, and $CD8^+$ T cells were significantly increased in the CHOL@GEM-NBs + US group compared with the other groups, suggesting that the combined therapy systematically enhances T cell immunity. Immunofluorescence was used to directly observe CRT and HMGB1 expression (Figure 8j). Consistent with the above in vitro results, the combination of CHOL@GEM-NBs and UTND enhanced intratumoral DAMPs release. According to the analysis of $CD8^+$ T cell infiltration into the tumor tissues (Figure 8j), many more $CD8^+$ T cells were observed in the CHOL@GEM-NBs + US group than in the other groups, which was consistent with the flow cytometry results. The above results showed that the combination of CHOL@GEM-NBs and UTND transformed "cold" tumors into immunologically "hot" tumors by recruiting $CD8^+$ T cells and reducing Tregs infiltration, further effectively inhibiting tumor growth.[46,47]

DISCUSSION

Pancreatic cancer is characterized by insidious onset, high lethality, and difficult early stage diagnosis. Its tumor microenvironment is highly immunosuppressive, severely limiting the therapeutic efficacy of chemotherapy and immunotherapeutic drugs in pancreatic cancer. Research has shown that pancreatic cancer cells with abnormally high NPC1L1 expression hijack cholesterol from $CD8^+$ T cells and impair their ability to evade immune surveillance.[48] Therefore, we prepared an integrated diagnostic and therapeutic drug-loaded nanobubble system (CHOL@GEM-NBs) to improve the tumor microenvironment and enhance the chemoimmunotherapeutic effect of GEM. By adding cholesterol components to the nanobubble shell, we actively targeted NPC1L1 in pancreatic cancer to enhance the effect of contrast-enhanced ultrasonography. As a carrier for chemotherapeutic drugs, NBs combined with ultrasound irradiation, can promote the local penetration and retention of GEM in tumors. Thus, this combination strategy effectively induces ICD, regulates cholesterol flow in the tumor microenvironment, promotes the infiltration of $CD8^+$ T cells, reduces Treg cells, effectively inhibits tumor growth, and enhances the antitumor effect.

Our study found that CHOL@GEM-NBs can specifically bind to pancreatic cancer cells, confirming its excellent active targeting ability. Therefore, adding cholesterol to the components of the nanobubble shell can promote its efficient aggregation on the tumor cell surface. The results of in vivo contrast-enhanced ultrasound showed that CHOL@GEM-NBs exhibited higher imaging intensity, longer imaging time, and larger area under the time−intensity curve in pancreatic tumors with high NPC1L1 expression. However, no differences were observed in the imaging parameters of CHOL@GEM-NBs and blank NBs in the tumors of the NPC1L1 KO group. This further indicates the dependence of the targeting property of CHOL@GEM-NBs on NPC1L1 expression, i.e., CHOL@GEM-NBs can specifically target NPC1L1 in tumor tissues.

As a chemotherapeutic drug carrier, CHOL@GEM-NBs can significantly improve the antitumor effect. In this study, the parameters of UTND were first optimized through in vitro experiments to exclude the influence of adverse thermal effects on cellular functions. After treatment with CHOL@GEM-NBs combined with ultrasound irradiation, the local accumulation of chemotherapeutic drugs in tumors were enhanced, and the growth of subcutaneous pancreatic cancer xenografts was significantly inhibited. It might suggest that cavitation and mechanical effects occurred during UTND.[49,50] The rupture of nanobubbles generated shear stress and shock waves, thus enhancing the permeability of the blood vessel wall and drug release.[51] Transient pores formed on the cell membrane, increasing the accumulation of chemotherapeutic drugs in cells.[52−56] Free GEM is rapidly decomposed into 2′,2′-difluoro-2′-deoxyuridine in vivo. In CHOL@GEM-NBs, GEM is covalently modified with CHOL-PEG2000-COOH, which not only enables active targeted delivery but also prevents degradation by cytidine-deaminase or water, improves the in vivo pharmacokinetics of GEM, and enhances the antitumor effect.[57,58] In summary, CHOL@GEM-NBs can actively target pancreatic cancer cells, deliver drugs in close proximity with these cells to reduce the adverse reactions caused by high-dose chemotherapy, minimize the impact on normal tissues, and improve the safety of this combined treatment strategy.

https://doi.org/10.1021/acsami.5c01194
ACS Appl. Mater. Interfaces 2025, 17, 34965−34981

Cholesterol is essential for maintaining the functions of $CD8^+$ T cells and natural killer cells, but NPC1L1 in tumor cells can competitively hijack cholesterol from $CD8^+$ T cells. As UTND has a synergistic effect on antitumor immunity, this study investigated the effects of combining CHOL@GEM-NBs combined with ultrasound irradiation in Panc02 cells. After treatment with CHOL@GEM-NBs combined with ultrasound irradiation, the cholesterol uptake ability of tumor cells decreased, indicating that the combined treatment blocked cholesterol flow in the tumor microenvironment and restored the antitumor function of $CD8^+$ T cells. Moreover, the combination treatment induced ICD in tumors and promoted the expression and release of DAMPs. The number of tumors infiltrating $CD8^+$ T cells and intracellular TNF-α cytokines increased while the Tregs decreased, indicating that this combined treatment strategy improved the tumor immune microenvironment and alleviated immunosuppression, providing an effective chemoimmunotherapeutic strategy for the treatment of pancreatic cancer.

CONCLUSIONS

In conclusion, we designed and developed ultrasound-targeted cholesterol-coated nanobubbles effectively loaded with the first-line chemotherapeutic drug gemcitabine (CHOL@GEM-NBs). The CHOL@GEM-NBs exhibited favorable stability and biocompatibility and enabled the targeting of pancreatic cancer cells with high NPC1L1 expression. This improved the local contrast of ultrasound molecular imaging and prolonged the imaging time, thereby improving pancreatic cancer diagnosis and progression monitoring. In addition, when combined with UTND, CHOL@GEM-NBs enhanced the retention of tumor penetration and drug uptake to effectively kill cancer cells, thereby inhibiting tumor growth and coordinating chemotherapy. This combined strategy mitigated cholesterol hijacking of tumor cells in the tumor microenvironment. In addition, the release of tumor-associated antigens and induction of ICD triggered the release of DAMPs, such as CRT and HMGB1. Essential cholesterol flow restoration and adaptive immunity activation improved the ITM, as evidenced by the increased infiltration of cytotoxic T lymphocytes, increased cytokine secretion, decreased Tregs proportion in tumor tissue and increased proportion of $CD45^+$, $CD3^+$, and $CD8^+$ T cells in the spleen and draining lymph nodes. Overall, this ultrasound-enhanced CHOL@GEM-NBs strategy presents a safe and stable multifunctional nanoplatform for the integrated diagnosis and chemoimmunotherapy of pancreatic cancer.

EXPERIMENTAL SECTION

Experimental Animals. C57BL/6 mice were purchased from Beijing HFK Bioscience Co. Ltd. (Beijing, China). Mice were kept in a specific pathogen-free environment with a temperature of 22 ± 1 °C, relative humidity varying from 40 to 60%, and a 12-h light/dark cycle featuring alternating illumination. All animal experiments complied with relevant laws and were certified by the Laboratory Animal Welfare and Ethics Committee of the Army Medical University (AMU-WEC20232227).

Synthesis of CHOL@GEM-NBs. 1,2-Dipalmitoyl-*sn*-glycero-3-phosphate (DPPA), 1,2-dipalmitoylsn-glycero-3-phosphocholine (DPPC), 1,2-dipalmitoyl-*sn*-glycero-3-phosphoethanolamine (DPPE), 1,2-dipalmitoyl-*sn*-glycero-3-phosphorylglycerol sodium salt (DPPG), 1,2-distearoyl-*sn*-glycero-3-phosphoethanolamine (DSPE), and 1,2-distearoyl-*sn*-glycero-3-phosphoethanolamine-N-[methoxy-(polyethylene glycol)-2000] (DSPE-PEG2000) were procured from Corden Pharma (Basel, Switzerland). Cholesterol-1,2-dimyristoyl-rac-glycero-3-methoxypolyethylene glycol-2000-gemcitabine (CHOL-PEG2000-GEM) was synthesized by Xi'an Ruixi Biological Technology Co. Ltd. (Xi'an City, China). DPPE, DPPC, DPPG, DPPA, and CHOL-PEG2000-GEM (fixed weight ratio of 3:3:3:1:1) were dissolved in a solution of PBS and glycerin (volume ratio of 9:1) under ultrasonication. The solution was placed in a vial, and the air within it was substituted with C3F8 gas (Research Institute of Physical and Chemical Engineering of Nuclear Industry, Tianjin, China). The solvent was vortexed using an HL-AH series amalgamator (Hangzhou Zhongrun Medical Instrument, Hangzhou, China) for 90 s at 3800 rpm, then stored at 4 °C. CHOL@GEM-NBs were obtained after separation by dispersion and differential centrifugation (300 r/min, 3 min, centrifugation: 5804R; Eppendorf, Hamburg, Germany). Blank NBs and CHOL@NBs without GEM were prepared by replacing DSPE-PEG2000 or adding cholesterol using the same method.

Characterization of CHOL@GEM-NBs. The morphology of CHOL@GEM-NBs was observed by optical microscopy (AX10 IMAGER.A2; ZEISS, Oberkochen, Germany) and a JEM1400 transmission electron microscope (JEOL, Tokyo, Japan) after negative staining with phosphotungstic acid. The NBs concentration was determined under a microscope using a hemocytometer. The particle size, polydispersity index, and zeta potential of CHOL@GEM-NBs and blank NBs were measured using a Malvern Zetasizer Nano ZSP detector (Malvern Instruments Inc., Malvern, UK) in an aqueous solution at 25 °C.

Encapsulation Rate and Drug Loading of CHOL@GEM-NBs. We used an ultraviolet spectrophotometer (ND200 Thermo Fisher Scientific, Waltham, MA, USA) to determine the absorption spectra and characteristic peaks of CHOL@GEM-NBs at various concentrations. A standard curve was established based on the absorption spectra of GEM at multiple concentrations. The absorption spectra of the encapsulated GEM were analyzed concerning a standard curve. The calculations were as follows:

$$\text{encapsulation efficiency}(\%) = (\text{encapsulated GEM})/(\text{total fed GEM}) \times 100\%$$

$$\text{loading efficiency}(\%) = (\text{encapsulated GEM})/(\text{total number of nanobubbles}) \times 100\%$$

Hemolysis Test. Fresh mouse blood subjected to heparin treatment was combined with a 10-fold volume of PBS and centrifuged at 2000 rpm for 10 min to acquire red blood cells. Blank NBs (1×10^7/mL, 5×10^7/mL, 1×10^8/mL, 5×10^8/mL, 1×10^8/mL), CHOL@GEM-NBs (1×10^7/mL, 5×10^7/mL, 1×10^8/mL, 5×10^8/mL, 1×10^8/mL), PBS (negative control), and 0.1% Triton X-100 (positive control) were jointly cultivated with 2% volume of red blood cells at 37 °C for 60 min. Following centrifugation at 10,000 rpm for 1 min to induce the precipitation of erythrocytes, snapshots of the samples were captured, and the absorbance of the supernatants at 545 nm was determined using a microplate reader (Varioskan Flash of Thermo Fisher Scientific).

Stability Assessment. Nanobubbles were maintained at 4 °C. To assess their stability, changes in the particle size and zeta potential of the CHOL@GEM-NBs were determined on days 0, 1, 2, 4, and 7.

In Vitro Ultrasound Imaging. A 1% agarose gel module was fabricated. Contrast-enhanced ultrasound images of CHOL@GEM-NBs at various concentrations (1×10^8, 5×10^7, 1×10^7, 5×10^6, and 1×10^6/mL) and blank NBs (5×10^7/mL) were obtained in this gel module and recorded using a small-animal imaging system (VEVO 2100; Visual sonics, Toronto, Canada) with a linear array probe (MS-250; frequency: 18 MHz) in vitro. CHOL@GEM-NBs were destroyed by applying 10 consecutive "manual flash" pulses. The in vitro ultrasound imaging intensity of all the NBs was measured using ImageJ software.

Cell Culture. Four cell lines (NPC1L1 knockout (KO) ovalbumin (OVA)-panc02, control OVA-panc02; NPC1L1 overexpression (OE) OVA-panc02; control panc02) and Panc02 murine pancreatic cancer cell lines were initially obtained from the American Type Culture

https://doi.org/10.1021/acsami.5c01194
ACS Appl. Mater. Interfaces 2025, 17, 34965−34981

Collection (Manassas, VI, USA). Cells were maintained in RPMI 1640 (GIBCO, Grand Island, NY, USA) supplemented with 10% fetal bovine serum (BI) and 1% Pen-Strep (GIBCO) at 37 °C in a humidified 5% CO_2 incubator.

NPC1L1 Expression in Tumor Cells. NPC1L1 KO, KO control, NPC1L1 OE, and OE control cells reaching a logarithmic phase were introduced into 24-well plates at 1×10^5 cells/dish and kept overnight for cultivation. Then, 4% buffered paraformaldehyde was used to fix the cells for ∼15 min, followed by blocking with 5% bovine serum albumin (BSA) for 1 h at 37 °C. The samples were incubated with rabbit antimurine NPC1L1 primary antibody (1:200) at 4 °C overnight, then treated with Alexa Fluor 488-labeled goat antirabbit secondary antibody in the dark for 1 h at room temperature. The cells were then washed with PBS and stained with DAPI for 5 min, and NPC1L1 expression in the cells was observed using a CLSM (LSM 780, ZEISS).

Targeting of CHOL@GEM-NBs. NPC1L1 KO, KO control, NPC1L1 OE, and OE control cells (1×10^5 cells/dish) were seeded in 24-well plates and incubated overnight. Subsequently, the cells were solidified with 4% paraformaldehyde for ∼15 min and blocked with 5% BSA−PBS for 1 h at 37 °C before being treated with DiI-labeled blank NBs and CHOL@GEM-NBs (5×10^7/mL) for 1 h, washed with PBS, and dyed with DAPI for 5 min. Finally, the targeted binding of blank NBs and CHOL@GEM-NBs to the cells was observed using a CLSM (LSM 780, ZEISS). To further validate the targeting ability of NBs, the cells were incubated with DiI-labeled NBs for 1 h and then digested. Thereafter, 12 samples were collected. The fluorescence signal of DiI in each group was detected using a NovoCyte ACEA flow cytometer. The relevant settings are as follows: channel selection was 561 nm PE-Texas Red, injection volume was 100 μL, sample flow diameter was 12.2 μm, and number of collected cells was 50,000.

In Vivo Ultrasound Imaging of NBs. Tumor-laden mice were anesthetized with isoflurane. Once the maximum transverse section of the tumor was presented by ultrasound, CHOL@GEM-NBs (100 μL, 5×10^8/mL) were injected through the posterior orbital venous sinus, and contrast ultrasound images were promptly and continuously captured at different times. Then, blank NBs (100 μL, 5×10^8/mL) were injected until the tumor intensity in the ultrasound images returned to the baseline level. Finally, the time to peak intensity, peak intensity, and area under the curve were analyzed on the time−intensity curve.

Screening Optimal Ultrasound Irradiation Conditions. Panc02 cells (5×10^3 cells/well) were plated into 96-well plates and incubated for 24 h, then treated under different ultrasound intensities (0, 0.5, 1.0, and 2.0 W/cm^2) and ultrasound irradiation times (0, 5, 10, 20, and 40 s). Alternatively, CHOL@GEM-NBs were added to the cells for 24 h at different concentrations (1×10^6, 5×10^6, 1×10^7, 5×10^7, 1×10^8, 5×10^8, 1×10^9, and 5×10^9/mL), and the cells were treated under different irradiation intensities (0.5, 1.0, and 2.0 W/cm^2; 20 s). The CCK-8 solution (5 mg/mL) was added to each well and cultivated for 1−2 h. Absorbance was measured at 450 nm using a microplate reader.

Cytotoxicity Evaluation of NBs In Vitro. Panc02 cells (1×10^5 cells/well) were plated into 24-well plates, incubated for 24 h, divided into the control, GEM, CHOL@GEM-NBs, CHOL@NBs, and CHOL@GEM-NBs + US groups, and treated accordingly. The ultrasound parameters were as follows (1 W/cm^2, 20 s, 5×10^7/mL). The treated cells were incubated for another 12 h. To observe the changes in the cytoskeleton after cell treatment, the cells were fixed in 4% paraformaldehyde for 15 min and permeabilized with 0.1% Triton X-100 for 20 min. The cells were then incubated with CoraLite594-conjugated goat antirabbit IgG (Proteintech, SA00013−4; 1:200) for 30 min. DAPI double staining and fluorescence microscopy were then performed. To observe the change in the proportion of living and dead cells after cell treatment, then stained with calcein−AM and PI. Fluorescence imaging of live and dead cells was performed using a CLSM. To observe the proportion of apoptosis induced by cell treatment, the treated cells were digested with EDTA-free trypsin, suspended in 195 μL binding buffer supplemented with 5 μL annexin V/FITC and 10 μL PI solution, mixed, and incubated in the dark for 5−15 min. The apoptosis level in each group was detected using flow cytometry.

In Vitro DAMPs and NPC1L1 Detection. Panc02 cells (1×10^5 cells/well) were seeded in 24-well plates and incubated for 24 h. The cells were then grouped for processing (control, GEM, CHOL@GEM-NBs, CHOL@NBs, and CHOL@GEM-NBs + US). Then, 0.1% Triton X-100 was added for 20 min of permeabilization. PBS with 5% BSA was added for 30 min to block the nonspecific binding sites. After washing with PBS, the cells were incubated with HMGB1 (ab79823, Abcam, Cambridge, UK), CRT (ab92516, Abcam), or NPC1L1 (PA1−16800, Invitrogen) antibody at 4 °C overnight. After washing again with PBS, the cells were incubated with Alexa Fluor 488-conjugated secondary antibodies in the dark for 1 h. The nuclei were stained with DAPI for 15 min and imaged using a CLSM.

Cellular Cholesterol Uptake. Panc02 cells (5×10^5 cells/well) were incubated overnight in six-well plates. The cells were treated with CHOL@GEM-NBs + US (1 W/cm^2, 20 s, 5×10^7/mL) and cultured for another 24 h. Untreated cells served as blank controls. After another 2 h of incubation with 40 ng/mL 22-NBD cholesterol (GC46527−500, GlpBio, Montclair, CA, USA), the cells were assessed by flow cytometry.

Distribution of CHOL@GEM-NBs in Tissues. After administering an anesthetic mixture of 3% halothane/O_2 for inhalation, Panc02 tumor-laden mice were randomly categorized (GEM, CHOL@GEM-NBs, and CHOL@GEM-NBs + US) and administered DiR-labeled GEM and CHOL@GEM-NBs (2 μg DiR/mouse, 100 μL) via the retro-orbital sinus. The ultrasound parameters were set at 1 MHz for 2 min. During the imaging process, the mice were anesthetized using 2% isoflurane/O_2 via inhalation. Fluorescence imaging was performed using an IVIS Spectrum CT (PerkinElmer, Shelton, CT, USA) at specific time points. After 30 min, the mice were euthanized, and fluorescence imaging of the major organs (heart, liver, spleen, lung, and kidney) and tumors was performed to determine the in vivo distribution and metabolism of NBs and their role in tumor biodistribution. Next, the distribution of CHOL@GEM-NBs were observed in frozen sections of the tumor. Briefly, Panc02 tumor-bearing mice were treated with DiI-labeled CHOL@GEM-NBs + US (2 μg DiI/mouse, 100 μL, 1 W/cm^2, 2 min). Tumor tissues were collected in a Tissue-Tek O.C.T. compound (SAKURA, St. Torrance, CA, USA), and 8 μm-thick frozen sections were fabricated at −20 °C (Leica CM195). After DAPI staining, the distribution of CHOL@GEM-NBs in tumor tissue was observed using a CLSM (LSM 780, ZEISS).

Synergistic Tumor Therapy. Tumor-laden mice were randomly categorized into five treatment groups ($n = 5$): control, GEM, CHOL@GEM-NBs, CHOL@NBs, and CHOL@GEM-NBs + US. PBS, GEM (2 mg/kg), and NBs were intravenously administered on days 7, 10, and 13. The mice were narcotized by 2% isoflurane/O_2 inhalation and subjected to postinjection ultrasound irradiation. The parameters were as follows: 1 W/cm^2, 2 min, 1 MHz, and a 60% duty cycle. Body weight and tumor volume were quantified every 2 days. After 12 days of observation, the mice were fasted for 8 h before euthanasia, and the tumors were excised and weighed. The tumor inhibition rate is calculated as follows:

$$\text{Tumor inhibition rate}(\%) = (W_1 - W_2)/W_1 \times 100\%$$

W_1 and W_2 represent the average weight of tumors in the control group and the treatment groups, respectively.

Histological Analysis. Following standard protocols, tumors were sliced and stained with H&E, immunohistochemistry, and immunofluorescence to assess the tumor necrosis, proliferation, apoptosis, and expression of $CD8^+$ T cells, CRT, and HMGB1.

In Vivo Biotoxicity. Routine hematological and biochemical analyses were performed on blood samples. Major organs (heart, liver, spleen, kidney, and lung) were immobilized with paraformaldehyde. The pathological status was evaluated using H&E staining.

Detection of Immune Cells. Tumor tissues were cut into small pieces, which were suspended in tumor digestion buffer containing 10% fetal bovine serum, 1 mg/mL collagenase IV, 0.1 mg/mL collagenase I, and 0.02 mg/mL DNase I. The tissues were incubated for 1 h on a 37 °C shaker. A 70 μm filter was employed to filter the cell suspension and

https://doi.org/10.1021/acsami.5c01194
ACS Appl. Mater. Interfaces 2025, 17, 34965−34981

obtain a single-cell suspension. Red blood cell lysis buffer was used to eliminate blood cells. Immune cells were labeled with corresponding surface-labeled antibodies, including anti-CD16/32, zombie NIR staining, lymphocytes ($CD45^+$), T cells ($CD45^+CD3^+$), tumor-infiltrating cytotoxic $CD8^+$ T lymphocytes ($CD45^+CD3^+CD8^+$) and helper $CD4^+$ T lymphocytes ($CD45^+CD3^+CD4^+$), programmed cell death protein 1 (PD-1), IFN-γ and TNF-α on T lymphocytes, and Tregs ($CD45^+CD3^+CD4^+foxp3^+$). The spleen and draining lymph nodes were ground to generate single-cell suspensions. The single-cell suspensions were filtered through a 70 μm filter and labeled with anti-CD16/32, zombie Nir, lymphocytes ($CD45^+$), T cells ($CD45^+CD3^+$), tumor-infiltrating cytotoxic $CD8^+$ T lymphocytes ($CD45^+CD3^+CD8^+$), helper $CD4^+$ T lymphocytes ($CD45^+CD3^+CD4^+$), and PD-1 on T lymphocytes. The antibodies used for flow cytometry were purchased from BioLegend (San Diego, CA, USA).

Statistical Analysis. Statistical analyses were performed using commercially available software (PRISM version 9.0.0; GraphPad Inc., San Diego, CA, USA). Data are presented as the mean ± standard deviation. A two-tailed Student's *t* test was used to identify significant differences between the two groups. A one-way analysis of variance (ANOVA) followed by the Bonferroni post hoc test was applied; for non-normally distributed data, the Kruskal–Wallis test, followed by Dunn's post hoc test, was used. For two-factor analyses, data were analyzed using two-way ANOVA followed by a Bonferroni post hoc test. A *P* value of less than 0.05 ($^*P < 0.05$) was deemed statistically significant. $^{**}P < 0.01$ and $^{***}P < 0.001$ denote significant differences. Ns denoted values that were not significant.

■ ASSOCIATED CONTENT

Supporting Information

The Supporting Information is available free of charge at https://pubs.acs.org/doi/10.1021/acsami.5c01194.

Chemical synthesis flowchart, structural information, standard curve, blood biochemical assessment, H&E staining, mouse body weight, binding specificity, flow cytometry gating strategy, $CD3^+$ T cells in tumor-infiltrating leukocytes, blood routine, contrast-enhanced ultrasound parameters (Figures S1–S10 and Tables S1–S3) (PDF)

■ AUTHOR INFORMATION

Corresponding Authors

Juanjuan Ou – *Department of Oncology and Southwest Cancer Centre, Southwest Hospital, Army Medical University, Chongqing 400038, China; Jinfeng Laboratory, Chongqing 401329, China*; Email: ojj521000@sina.com

Yanli Guo – *Department of Ultrasound, Southwest Hospital, Army Medical University, Chongqing 400038, China*; orcid.org/0000-0003-1685-4441; Email: guoyanli@tmmu.edu.cn

Authors

Li Dong – *Department of Ultrasound, Southwest Hospital, Army Medical University, Chongqing 400038, China*

Deng Liu – *Department of Ultrasound, Southwest Hospital, Army Medical University, Chongqing 400038, China*; orcid.org/0000-0003-0939-4176

Jun Zhang – *Department of Ultrasound, Southwest Hospital, Army Medical University, Chongqing 400038, China*

Yi Ling – *Department of Ultrasound, Southwest Hospital, Army Medical University, Chongqing 400038, China*

Xin Li – *Department of Ultrasound, Southwest Hospital, Army Medical University, Chongqing 400038, China*

Complete contact information is available at: https://pubs.acs.org/10.1021/acsami.5c01194

Author Contributions

L.D. and D.L. contributed equally to this work. The manuscript was written through contributions of all authors. All authors have given approval to the final version of the manuscript.

Notes

The authors declare no competing financial interest.

■ ACKNOWLEDGMENTS

The authors acknowledge the funding support from the National Natural Science Foundation of China (No. 82171956) and the Key Technology Innovation Special of Key Industries of the Chongqing Science and Technology Bureau, China (No. CSTB2022TIAD-KPX0153).

■ ABBREVIATIONS

AM, acetoxymethyl; ANOVA, analysis of variance; BSA, bovine serum albumin; CHOL@GEM-NBs, cholesterol-coated nanobubbles loaded with gemcitabine; CHOL-PEG2000-GEM, cholesterol-1,2-dimyristoyl-rac-glycero-3-methoxypolyethylene glycol-2000-gemcitabine; CLSM, confocal laser microscope; CRT, calreticulin; DAMPs, damage-associated molecular patterns; DPPA, 1,2-dipalmitoyl-*sn*-glycero-3-phosphate; DPPC, 1,2-dipalmitoylsn-glycero-3-phosphocholine; DPPE, 1,2-dipalmitoyl-*sn*-glycero-3-phosphoethanolamine; DPPG, 1,2-dipalmitoyl-*sn*-glycero-3-phosphorylglycerol sodium salt; DSPE, 1,2-distearoyl-*sn*-glycero-3-phosphoethanolamine; DSPE-PEG2000, 1,2-distearoyl-*sn*-glycero-3-phosphoethanolamine-N-[methoxy(polyethylene glycol)-2000; GEM, gemcitabine; H&E, hematoxylin and eosin; HMGB1, high-mobility group box 1; ICD, immunogenic cell death; ITM, immunosuppressive tumor microenvironment; NPC1L1, Niemann-Pick C1-like 1; PBS, phosphate-buffered saline; PI, propidium iodide; Tregs, regulatory T cells; UTND, ultrasound-targeted nanobubble destruction

■ REFERENCES

(1) Connor, A. A.; Gallinger, S. Pancreatic Cancer Evolution and Heterogeneity: Integrating Omics and Clinical Data. *Nat. Rev. Cancer* **2022**, *22* (3), 131–142.

(2) Kleeff, J.; Korc, M.; Apte, M.; La Vecchia, C.; Johnson, C. D.; Biankin, A. V.; Neale, R. E.; Tempero, M.; Tuveson, D. A.; Hruban, R. H.; Neoptolemos, J. P. Pancreatic Cancer. *Nat. Rev. Dis Primers* **2016**, *2* (1), 1–22.

(3) Principe, D. R.; Underwood, P. W.; Korc, M.; Trevino, J. G.; Munshi, H. G.; Rana, A. The Current Treatment Paradigm for Pancreatic Ductal Adenocarcinoma and Barriers to Therapeutic Efficacy. *Front Oncol* **2021**, *11*, No. 688377.

(4) Hu, Z. I.; O'Reilly, E. M. Therapeutic Developments in Pancreatic Cancer. *Nat. Rev. Gastroenterol Hepatol* **2024**, *21* (1), 7–24.

(5) Klotz, R.; Doerr-Harim, C.; Ahmed, A.; Tjaden, C.; Tarpey, M.; Diener, M. K.; Hackert, T.; Mihaljevic, A. L. Top Ten Research Priorities for Pancreatic Cancer Therapy. *Lancet Oncol* **2020**, *21* (6), e295–e296.

(6) Chiaro, M. D.; Sugawara, T.; Karam, S. D.; Messersmith, W. A. Advances in the Management of Pancreatic Cancer. *BMJ* **2023**, *383*, No. e073995.

(7) Natu, J.; Nagaraju, G. P. Gemcitabine Effects on Tumor Microenvironment of Pancreatic Ductal Adenocarcinoma: Special Focus on Resistance Mechanisms and Metronomic Therapies. *Cancer Lett.* **2023**, *573*, No. 216382.

(8) Ju, Y.; Xu, D.; Liao, M.; Sun, Y.; Bao, W.; Yao, F.; Ma, L. Barriers and Opportunities in Pancreatic Cancer Immunotherapy. *npj Precis. Onc.* **2024**, *8* (1), 1–18.

(9) Kidani, Y.; Elsaesser, H.; Hock, M. B.; Vergnes, L.; Williams, K. J.; Argus, J. P.; Marbois, B. N.; Komisopoulou, E.; Wilson, E. B.; Osborne, T. F.; Graeber, T. G.; Reue, K.; Brooks, D. G.; Bensinger, S. J. Sterol Regulatory Element−Binding Proteins Are Essential for the Metabolic Programming of Effector T Cells and Adaptive Immunity. *Nat. Immunol* **2013**, *14* (5), 489−499.
(10) Yu, S.; Wang, L.; Che, D.; Zhang, M.; Li, M.; Naito, M.; Xin, W.; Zhou, L. Targeting CRABP-II Overcomes Pancreatic Cancer Drug Resistance by Reversing Lipid Raft Cholesterol Accumulation and AKT Survival Signaling. *J. Exp Clin Cancer Res.* **2022**, *41* (1), 88.
(11) King, R. J.; Singh, P. K.; Mehla, K. The Cholesterol Pathway: Impact on Immunity and Cancer. *Trends Immunol* **2022**, *43* (1), 78−92.
(12) Ma, X.; Bi, E.; Lu, Y.; Su, P.; Huang, C.; Liu, L.; Wang, Q.; Yang, M.; Kalady, M. F.; Qian, J.; Zhang, A.; Gupte, A. A.; Hamilton, D. J.; Zheng, C.; Yi, Q. Cholesterol Induces CD8+ T-Cell Exhaustion in the Tumor Microenvironment. *Cell Metab.* **2019**, *30* (1), 143−156.e5.
(13) Yan, C.; Zheng, L.; Jiang, S.; Yang, H.; Guo, J.; Jiang, L.; Li, T.; Zhang, H.; Bai, Y.; Lou, Y.; Zhang, Q.; Liang, T.; Schamel, W.; Wang, H.; Yang, W.; Wang, G.; Zhu, Z.; Song, B.-L.; Xu, C. Exhaustion-Associated Cholesterol Deficiency Dampens the Cytotoxic Arm of Antitumor Immunity. *Cancer Cell* **2023**, *41* (7), 1276−1293.e11.
(14) Yang, W.; Bai, Y.; Xiong, Y.; Zhang, J.; Chen, S.; Zheng, X.; Meng, X.; Li, L.; Wang, J.; Xu, C.; Yan, C.; Wang, L.; Chang, C. C. Y.; Chang, T.-Y.; Zhang, T.; Zhou, P.; Song, B.-L.; Liu, W.; Sun, S.; Liu, X.; Li, B.; Xu, C. Potentiating the Antitumour Response of CD8+ T Cells by Modulating Cholesterol Metabolism. *Nature* **2016**, *531* (7596), 651−655.
(15) Liu, J.; Bai, Y.; Li, Y.; Li, X.; Luo, K. Reprogramming the Immunosuppressive Tumor Microenvironment through Nanomedicine: An Immunometabolism Perspective. *eBioMedicine* **2024**, *107*, No. 105301.
(16) Wu, H.; Wu, X.; Zhao, M.; Yan, J.; Li, C.; Zhang, Z.; Tang, S.; Wang, R.; Fei, W. Regulating Cholesterol in Tumorigenesis: A Novel Paradigm for Tumor Nanotherapeutics. *Int. J. Nanomed.* **2024**, *19*, 1055−1076.
(17) Luo, J.; Yang, H.; Song, B.-L. Mechanisms and Regulation of Cholesterol Homeostasis. *Nat. Rev. Mol. Cell Biol.* **2020**, *21* (4), 225−245.
(18) Li, P.-S.; Fu, Z.-Y.; Zhang, Y.-Y.; Zhang, J.-H.; Xu, C.-Q.; Ma, Y.-T.; Li, B.-L.; Song, B.-L. The Clathrin Adaptor Numb Regulates Intestinal Cholesterol Absorption through Dynamic Interaction with NPC1L1. *Nat. Med.* **2014**, *20* (1), 80−86.
(19) Altmann, S. W.; Davis, H. R.; Zhu, L.; Yao, X.; Hoos, L. M.; Tetzloff, G.; Iyer, S. P. N.; Maguire, M.; Golovko, A.; Zeng, M.; Wang, L.; Murgolo, N.; Graziano, M. P. Niemann-Pick C1 Like 1 Protein Is Critical for Intestinal Cholesterol Absorption. *Science* **2004**, *303* (5661), 1201−1204.
(20) Nicolle, R.; Blum, Y.; Marisa, L.; Loncle, C.; Gayet, O.; Moutardier, V.; Turrini, O.; Giovannini, M.; Bian, B.; Bigonnet, M.; Rubis, M.; Elarouci, N.; Armenoult, L.; Ayadi, M.; Duconseil, P.; Gasmi, M.; Ouaissi, M.; Maignan, A.; Lomberk, G.; Boher, J.-M.; Ewald, J.; Bories, E.; Garnier, J.; Goncalves, A.; Poizat, F.; Raoul, J.-L.; Secq, V.; Garcia, S.; Grandval, P.; Barraud-Blanc, M.; Norguet, E.; Gilabert, M.; Delpero, J.-R.; Roques, J.; Calvo, E.; Guillaumond, F.; Vasseur, S.; Urrutia, R.; de Reyniès, A.; Dusetti, N.; Iovanna, J. Pancreatic Adenocarcinoma Therapeutic Targets Revealed by Tumor-Stroma Cross-Talk Analyses in Patient-Derived Xenografts. *Cell Rep* **2017**, *21* (9), 2458−2470.
(21) Wegierak, D.; Cooley, M. B.; Perera, R.; Wulftange, W. J.; Gurkan, U. A.; Kolios, M. C.; Exner, A. A. Decorrelation Time Mapping as an Analysis Tool for Nanobubble-Based Contrast Enhanced Ultrasound Imaging. *IEEE Trans Med. Imaging* **2024**, *43* (6), 2370−2380.
(22) Batchelor, D. V. B.; Armistead, F. J.; Ingram, N.; Peyman, S. A.; McLaughlan, J. R.; Coletta, P. L.; Evans, S. D. The Influence of Nanobubble Size and Stability on Ultrasound Enhanced Drug Delivery. *Langmuir* **2022**, *38* (45), 13943−13954.
(23) Ramirez, D. G.; Abenojar, E.; Hernandez, C.; Lorberbaum, D. S.; Papazian, L. A.; Passman, S.; Pham, V.; Exner, A. A.; Benninger, R. K. P. Contrast-Enhanced Ultrasound with Sub-Micron Sized Contrast Agents Detects Insulitis in Mouse Models of Type1 Diabetes. *Nat. Commun.* **2020**, *11* (1), 2238.
(24) Krysko, D. V.; Garg, A. D.; Kaczmarek, A.; Krysko, O.; Agostinis, P.; Vandenabeele, P. Immunogenic Cell Death and DAMPs in Cancer Therapy. *Nat. Rev. Cancer* **2012**, *12* (12), 860−875.
(25) Ren, E.; Wang, Y.; Liang, T.; Zheng, H.; Shi, J.; Cheng, Z.; Li, H.; Gu, Z. Local Drug Delivery Techniques for Triggering Immunogenic Cell Death. *Small Methods* **2023**, *7* (9), 2300347.
(26) Hu, J.; He, J.; Wang, Y.; Zhao, Y.; Fang, K.; Dong, Y.; Chen, Y.; Zhang, Y.; Zhang, C.; Wang, H.; Tan, J.; Wang, J.; Zi, R.; Liu, C.; Liang, H.; Guo, Y.; Ou, J. Ultrasound Combined with Nanobubbles Promotes Systemic Anticancer Immunity and Augments Anti-PD1 Efficacy. *J. Immunother Cancer* **2022**, *10* (3), No. e003408.
(27) Salas-Benito, D.; Pérez-Gracia, J. L.; Ponz-Sarvisé, M.; Rodriguez-Ruiz, M. E.; Martínez-Forero, I.; Castañón, E.; López-Picazo, J. M.; Sanmamed, M. F.; Melero, I. Paradigms on Immunotherapy Combinations with Chemotherapy. *Cancer Discovery* **2021**, *11* (6), 1353−1367.
(28) Wang, J.; Yang, J.; Narang, A.; He, J.; Wolfgang, C.; Li, K.; Zheng, L. Consensus, Debate, and Prospective on Pancreatic Cancer Treatments. *J. Hematol Oncol* **2024**, *17* (1), 92.
(29) Liu, S.; Zhang, Y.; Liu, Y.; Wang, W.; Gao, S.; Yuan, W.; Sun, Z.; Liu, L.; Wang, C. Ultrasound-Targeted Microbubble Destruction Remodels Tumour Microenvironment to Improve Immunotherapeutic Effect. *Br. J. Cancer* **2023**, *128* (5), 715−725.
(30) Li, J.; Xi, A.; Qiao, H.; Liu, Z. Ultrasound-Mediated Diagnostic Imaging and Advanced Treatment with Multifunctional Micro/Nanobubbles. *Cancer Letters* **2020**, *475*, 92−98.
(31) Dehariya, D.; Eswar, K.; Tarafdar, A.; Balusamy, S.; Rengan, A. K. Recent Advances of Nanobubble-Based Systems in Cancer Therapeutics: A Review. *Biomed Eng. Adv.* **2023**, *5*, No. 100080.
(32) Wang, T.; Wang, Y.; Liu, T.; Yu, F.; Liu, L.; Xiong, H.; Xu, W.; Fan, X.; Liu, X.; Jiang, H.; Zhang, H.; Wang, X. Potentiating Immunogenic Cell Death in Cold Tumor with Functional Living Materials of FeAu-Methylene Blue Composites. *Adv. Healthc Mater.* **2024**, *13* (14), 2302767.
(33) Exner, A. A.; Kolios, M. C. Bursting Microbubbles: How Nanobubble Contrast Agents Can. Enable the Future of Medical Ultrasound Molecular Imaging and Image-Guided Therapy. *Curr. Opin. Colloid Interface Sci.* **2021**, *54*, No. 101463.
(34) Chowdhury, S. M.; Abou-Elkacem, L.; Lee, T.; Dahl, J.; Lutz, A. M. Ultrasound and Microbubble Mediated Therapeutic Delivery: Underlying Mechanisms and Future Outlook. *J. Control. Release* **2020**, *326*, 75−90.
(35) Song, X.; Zhang, Q.; Chang, M.; Ding, L.; Huang, H.; Feng, W.; Xu, T.; Chen, Y. Nanomedicine-Enabled Sonomechanical, Sonopiezoelectric, Sonodynamic, and Sonothermal Therapy. *Adv. Mater.* **2023**, *35* (31), 2212259.
(36) Codini, M.; Garcia-Gil, M.; Albi, E. Cholesterol and Sphingolipid Enriched Lipid Rafts as Therapeutic Targets in Cancer. *Int. J. Mol. Sci.* **2021**, *22* (2), 726.
(37) Liu, Y.; Niu, R.; Deng, R.; Wang, Y.; Song, S.; Zhang, H. Multi-Enzyme Co-Expressed Nanomedicine for Anti-Metastasis Tumor Therapy by Up-Regulating Cellular Oxidative Stress and Depleting Cholesterol. *Adv. Mater.* **2024**, *36* (2), 2307752.
(38) Li, X.; Hou, W.; Xiao, C.; Yang, H.; Zhao, C.; Cao, D. Panoramic Tumor Microenvironment in Pancreatic Ductal Adenocarcinoma. *Cell Oncol* **2024**, *47* (5), 1561−1578.
(39) Sun, C.; Zhan, J.; Li, Y.; Zhou, C.; Huang, S.; Zhu, X.; Huang, K. Non-apoptotic Regulated Cell Death Mediates Reprogramming of the Tumour Immune Microenvironment by Macrophages. *J. Cell Mol. Med.* **2024**, *28* (8), No. e18348.
(40) Chen, Q.; Li, C.; Wang, Q. Multifunctional Nano-Biomaterials for Cancer Therapy via Inducing Enhanced Immunogenic Cell Death. *Small Methods* **2023**, *7* (5), 2201457.

https://doi.org/10.1021/acsami.5c01194
ACS Appl. Mater. Interfaces 2025, 17, 34965−34981

(41) Luo, W.; Wang, J.; Chen, H.; Qiu, J.; Wang, R.; Liu, Y.; Su, D.; Tao, J.; Weng, G.; Ma, H.; Zhang, T. Novel Strategies Optimize Immunotherapy by Improving the Cytotoxic Function of T Cells for Pancreatic Cancer Treatment. *Cancer Lett.* **2023**, *576*, No. 216423.
(42) Carstens, J. L.; Correa de Sampaio, P.; Yang, D.; Barua, S.; Wang, H.; Rao, A.; Allison, J. P.; LeBleu, V. S.; Kalluri, R. Spatial Computation of Intratumoral T Cells Correlates with Survival of Patients with Pancreatic Cancer. *Nat. Commun.* **2017**, *8* (1), 15095.
(43) Ryan, A. T.; Kim, M.; Lim, K. Immune Cell Migration to Cancer. *Cells* **2024**, *13* (10), 844.
(44) Joseph, A. M.; Al Aiyan, A.; Al-Ramadi, B.; Singh, S. K.; Kishore, U. Innate and Adaptive Immune-Directed Tumour Microenvironment in Pancreatic Ductal Adenocarcinoma. *Front Immunol* **2024**, *15*, 15.
(45) Steele, N. G.; Carpenter, E. S.; Kemp, S. B.; Sirihorachai, V. R.; The, S.; Delrosario, L.; Lazarus, J.; Amir, E. D.; Gunchick, V.; Espinoza, C.; Bell, S.; Harris, L.; Lima, F.; Irizarry-Negron, V.; Paglia, D.; Macchia, J.; Chu, A. K. Y.; Schofield, H.; Wamsteker, E.-J.; Kwon, R.; Schulman, A.; Prabhu, A.; Law, R.; Sondhi, A.; Yu, J.; Patel, A.; Donahue, K.; Nathan, H.; Cho, C.; Anderson, M. A.; Sahai, V.; Lyssiotis, C. A.; Zou, W.; Allen, B. L.; Rao, A.; Crawford, H. C.; Bednar, F.; Frankel, T. L.; Pasca Di Magliano, M. Multimodal Mapping of the Tumor and Peripheral Blood Immune Landscape in Human Pancreatic Cancer. *Nat. Cancer* **2020**, *1* (11), 1097−1112.
(46) Galon, J.; Bruni, D. Approaches to Treat Immune Hot, Altered and Cold Tumours with Combination Immunotherapies. *Nat. Rev. Drug Discov* **2019**, *18* (3), 197−218.
(47) Orhan, A.; Vogelsang, R. P.; Andersen, M. B.; Madsen, M. T.; Hölmich, E. R.; Raskov, H.; Gögenur, I. The Prognostic Value of Tumour-Infiltrating Lymphocytes in Pancreatic Cancer: A Systematic Review and Meta-Analysis. *Eur. J. Cancer* **2020**, *132*, 71−84.
(48) Zi, R.; Shen, K.; Zheng, P.; Su, X.; Yang, Y.; Chen, Y.; Dai, H.; Mao, C.; Lu, Y.; Wang, L.; Ma, H.; Wang, W.; Li, Q.; Lu, W.; Li, C.; Zheng, S.; Shi, H.; Liu, X.; Chen, Z.; Liang, H.; Ou, J. NPC1L1 on Pancreatic Adenocarcinoma Cell Functions as a Two-Pronged Checkpoint against Antitumor Activity. The. *Innovation* **2025**, *6*, No. 100783.
(49) Zhang, S.; Li, E.; Liu, Z.; Shang, H.; Chen, Y.; Jing, H. Nanoparticle-Based Olaparib Delivery Enhances Its Effect, and Improves Drug Sensitivity to Cisplatin in Triple Negative Breast Cancer. *Journal of Drug Delivery Science and Technology* **2022**, *76*, No. 103731.
(50) Yu, Z.; Wang, Y.; Xu, D.; Zhu, L.; Hu, M.; Liu, Q.; Lan, W.; Jiang, J.; Wang, L. G250 Antigen-Targeting Drug-Loaded Nanobubbles Combined with Ultrasound Targeted Nanobubble Destruction: A Potential Novel Treatment for Renal Cell Carcinoma. *IJN* **2020**, *15*, 81−95.
(51) Shinar, H.; Ilovitsh, T. Volumetric Passive Acoustic Mapping and Cavitation Detection of Nanobubbles under Low-Frequency Insonation. *ACS Mater. Au* **2025**, *5* (1), 159−169.
(52) Nittayacharn, P.; Abenojar, E.; Cooley, M. B.; Berg, F. M.; Counil, C.; Sojahrood, A. J.; Khan, M. S.; Yang, C.; Berndl, E.; Golczak, M.; Kolios, M. C.; Exner, A. A. Efficient Ultrasound-Mediated Drug Delivery to Orthotopic Liver Tumors−Direct Comparison of Doxorubicin-Loaded Nanobubbles and Microbubbles. *J. Controlled Release* **2024**, *367*, 135−147.
(53) Qian, X.; Wang, Y.; Xu, Y.; Ma, L.; Xue, N.; Jiang, Z.; Cao, Y.; Akakuru, O. U.; Li, J.; Zhang, S.; Wu, A. Active Targeting Nano-Scale Bubbles Enhanced Ultrasound Cavitation Chemotherapy in Y1 Receptor-Overexpressed Breast Cancer. *J. Mater. Chem. B* **2020**, *8* (31), 6837−6844.
(54) Guo, X.; Lin, J.; Pan, L.; He, K.; Huang, Z.; Chen, J.; Lin, C.; Zeng, B.; Luo, S.; Wang, M. Ultrasound-Triggered Release of miR-199a-3p from Liposome Nanobubbles for Enhanced Hepatocellular Carcinoma Treatment. *Artificial Cells, Nanomedicine, and Biotechnology* **2023**, *51* (1), 560−571.
(55) Liu, D.; Ling, Y.; Dong, L.; Zhang, J.; Li, X.; Chen, X.; Huang, H.; Deng, J.; Guo, Y. Ultrasound-Triggered Drug-Loaded Nanobubbles for Enhanced T Cell Recruitment in Cancer Chemoimmunotherapy. *Biomaterials* **2025**, *317*, No. 123086.
(56) Li, H.; Lv, W.; Zhang, Y.; Feng, Q.; Wu, H.; Su, C.; Shu, H.; Nie, F. PLGA-PEI Nanobubbles Carrying PDLIM5 siRNA Inhibit EGFR-TKI-Resistant NSCLC Cell Migration and Invasion Ability Using UTND Technology. *Journal of Drug Delivery Science and Technology* **2023**, *82*, No. 104346.
(57) Han, H.; Valdepérez, D.; Jin, Q.; Yang, B.; Li, Z.; Wu, Y.; Pelaz, B.; Parak, W. J.; Ji, J. Dual Enzymatic Reaction-Assisted Gemcitabine Delivery Systems for Programmed Pancreatic Cancer Therapy. *ACS Nano* **2017**, *11* (2), 1281−1291.
(58) Yin, L.; Ren, T.; Zhao, S.; Shi, M.; Gu, J. Comparative Pharmacokinetic Study of PEGylated Gemcitabine and Gemcitabine in Rats by LC-MS/MS Coupled with Pre-Column Derivatization and MSALL Technique. *Talanta* **2020**, *206*, No. 120184.

https://doi.org/10.1021/acsami.5c01194
ACS Appl. Mater. Interfaces 2025, 17, 34965−34981